Compressive shear faults within arctic sea ice: Fracture on scales large and small

Erland M. Schulson

Ice Research Laboratory, Thayer School of Engineering, Dartmouth College, Hanover, New Hampshire, USA

Received 26 August 2003; revised 16 April 2004; accepted 24 May 2004; published 22 July 2004.

[1] We examined fracture features within arctic sea ice as revealed by Landsat-7 and RADARSAT imagery, by an aerial survey, and through observations in the laboratory of specimens loaded to brittle failure under biaxial compression. Regardless of scale, which spans the range from kilometers to millimeters, the features look alike. They consist mainly of narrow lineaments that traverse the field of view, plus wing-like and comb-like secondary cracks. The lineaments occasionally intersect and generally exhibit either right-lateral or left-lateral relative movement, like strike-slip faults within Earth's crust. We term them brittle compressive shear faults. They form through the linking of en echelon arrays of deformation-induced secondary cracks. From an application of wing-crack and comb-crack mechanics, we estimated the maximum compressive stress near the onset of faulting and found that our estimates compare favorably with in situ measurements by earlier investigators of ice sheet failure stresses. To account for the brittle behavior of the sea ice cover, we applied a recent model of the ductile-to-brittle transition in which the key idea is the competition between stress buildup and stress relaxation at stress concentrators. In identifying the nature of sea ice fracture features, we advance the view that failure occurs on many scales through highly localized as opposed to uniformly distributed deformation, via the operation of scale-independent mechanisms. *INDEX TERMS:* 4540 Oceanography: Physical: Ice mechanics and air/sea/ice exchange processes; 5104 Physical Properties of Rocks: Fracture and flow; 6020 Planetology: Comets and Small Bodies: Ice; 8010 Structural Geology: Fractures and faults; *KEYWORDS:* compressive faults, arctic sea ice, fracture

Citation: Schulson, E. M. (2004), Compressive shear faults within arctic sea ice: Fracture on scales large and small, *J. Geophys. Res.*, *109*, C07016, doi:10.1029/2003JC002108.

1. Introduction

[2] In this paper we examine the nature of fracture features that form during winter within the sea ice cover on the Arctic Ocean, within the seasonal and the perennial ice zones. The dominant ones, and the focus of this paper, appear as narrow lineaments on satellite imagery [*Marko and Thomson*, 1977; *Erlingsson*, 1988; *Walter and Overland*, 1993; *Kwok et al.*, 1995; *Lindsay and Rothrock*, 1995; *Overland et al.*, 1995; *Stern and Rothrock*, 1995; *Walter et al.*, 1995; *Kwok*, 1998; *Overland et al.*, 1998; *Kwok*, 2001; *Richter-Menge et al.*, 2002; *Stern and Moritz*, 2002] and often run hundreds and occasionally thousands of kilometers through the cover. Sometimes they intersect in an acute angle (typically $2\theta \sim 20^\circ$ to 40°) to form diamond-shaped patterns that appear to be independent of spatial scale [*Walter et al.*, 1995], at least over the range 10–150 km. Lineaments mark zones where velocity gradients are spatially discontinuous [*Kwok et al.*, 1995; *Stern and Rothrock*, 1995; *Kwok*, 1998] and, thus, where shear and/or divergence as well as vorticity are concentrated. For this reason, they have been termed "slip lines" [*Erlingsson*, 1988; *Overland et al.*, 1998] and, less specifically, "linear kinematic features" [*Kwok*, 2001]. In effect, lineaments divide the cover into semi-rigid plates or parts of plates, which move apart or wedge open to allow new ice to grow and then move together to create pressure ridges. The relative movement affects the ice thickness distribution and hence the heat flux from the ocean to the atmosphere [*Maykut*, 1982], while the growth of new ice affects the oceanic salt flux. In other words, sea ice lineaments are a significant deformation feature with respect to arctic climate [*Zhang et al.*, 2000; *Vavrus and Harrison*, 2003]. How they form is the issue.

[3] We present some new observations of fracture features within arctic sea ice, and then offer an interpretation and an analysis based upon crack mechanics. We consider first a high-resolution Landsat-7 image of long lineaments and a RADARSAT companion, and then compare them to observations of cracks seen from a Twin Otter aircraft. Next, we show that the field features resemble shear faults and secondary cracks that mark terminal failure of small test specimens when deformed under biaxial compression within the regime of brittle behavior. From fracture mechanics, we estimate the maximum principal stress under which cracks formed in the sea ice cover, and show that the

0148-0227/04/2003JC002108$09.00

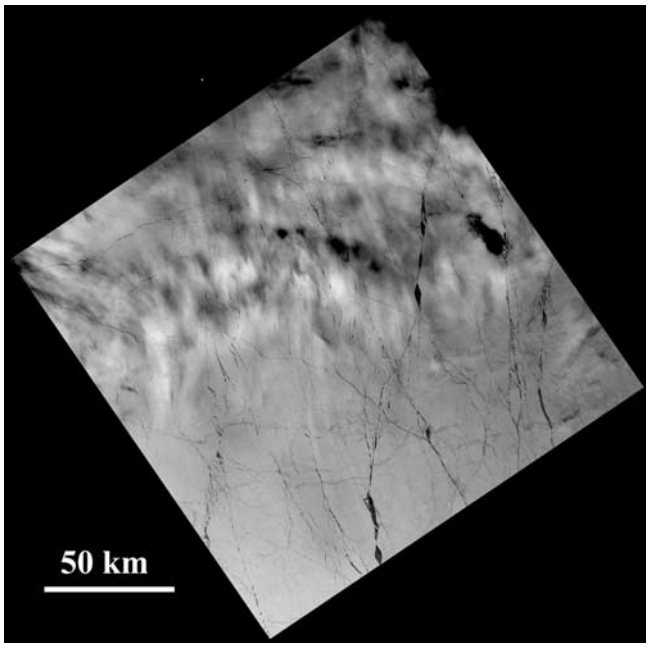

Figure 1a. Landsat-7 image of the sea ice cover on the Beaufort Sea, 25 March 2000, centered approximately at 80.0°N/135.7°W. North is up. Pixel size is 29 m. The spatial scale is an average of the horizontal and vertical scales (see text).

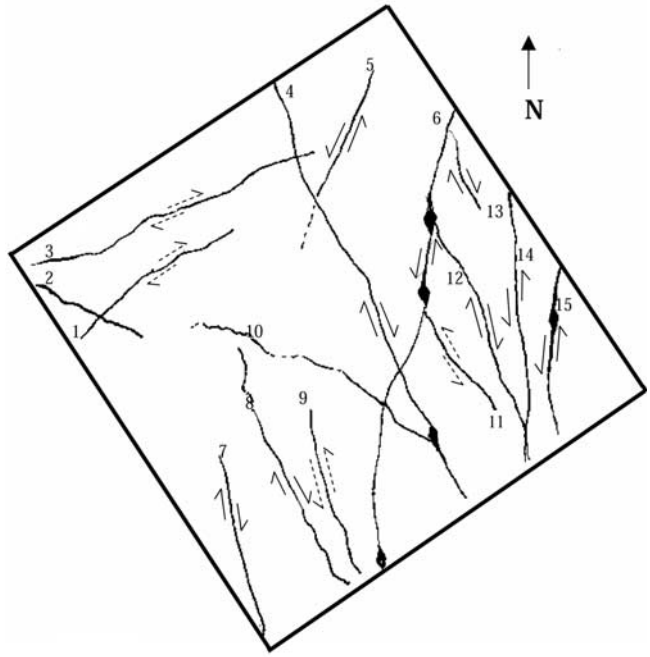

Figure 1b. Schematic sketch of Figure 1a where the most prominent lineaments are labeled L1–L15. The arrows denote either right-lateral or left-lateral relative movement.

estimates compare favorably to in situ measurements of failure stresses by *Richter-Menge and Elder* [1998] and *Richter-Menge et al.* [2002]. We then describe a mechanism in which sliding lineaments/shear faults are initiated through the interaction of deformation-induced secondary cracks, and we show other RADARSAT images and cite measured stresses that support the mechanism. In accord with earlier observations [*Schulson and Hibler*, 1991] and with recent scaling analysis [*Weiss*, 2001, 2003] and numerical modeling [*Hibler and Schulson*, 2000; *Hutchings and Hibler*, 2002], we argue that over the range of spatial scales and conditions investigated, the physics of fracture seem to be independent of scale.

2. Observations

2.1. Landsat-7 Images

[4] Figure 1a shows an image of 29 m pixel size that was produced on 25 March 2000 by Landsat-7, within the visible band. We discovered it by reviewing the Landsat-7 archives (http://landsat7.usgs.gov/index.html) for the Beaufort Sea from April 1999 to January 2002. The scene is within the pack ice near the Canadian Archipelago, Figure 1c, and its latitude and longitude coordinates are UL 81.09°N/143.27°W, UR 81.12°N/128.25°W, LL 78.80°N/141.59°W, LR 78.83°N/129.63°W. The image encompasses an area 183 km wide (ENE–WSW axis) × 170 long (NNW–SSE axis).

[5] Of primary interest are the long lineaments. They appear dark because they delineate zones of low albedo associated with either open water or thinner ice. Fifteen of the more prominent ones are sketched in Figure 1b. (Although labeled separately, L2 and L10 may be part of the same fracture zone.) Lineaments L4–L9 and L11–L15 possess a strong N–S component to their orientation, while lineaments L1–L3 and L10 have a strong E–W component. Three multikilometer-sized rhomboidal-shaped openings appear on L6, one on L15, and a deformed one on the southern segment of L4. Smaller rhomboids decorate the other lineaments (Figure 2), except L2 and L10 on which none was seen. While the lineaments per se indicate localized divergence, the rhomboids indicate relative shear displacement. The displacement is of right-lateral or R-L character for the subparallel set composed of L4, L7, L8, L12, and L13 and of left-lateral or L-L character for the subparallel set composed of L5, L6, L14, and L15, where the handedness is defined in Figure 3 and is apparent from Figure 2. R-L displacement is also evident along L1 and L3 (Figures 2a and 2b), which are almost orthogonal to the first

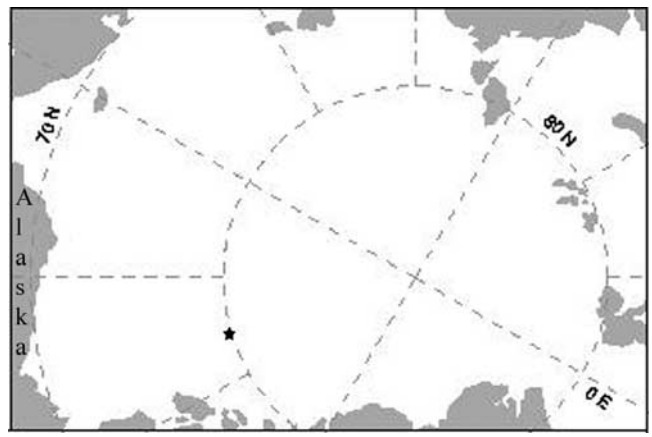

Figure 1c. Showing the location (asterisk) of the scene in the Beaufort Sea.

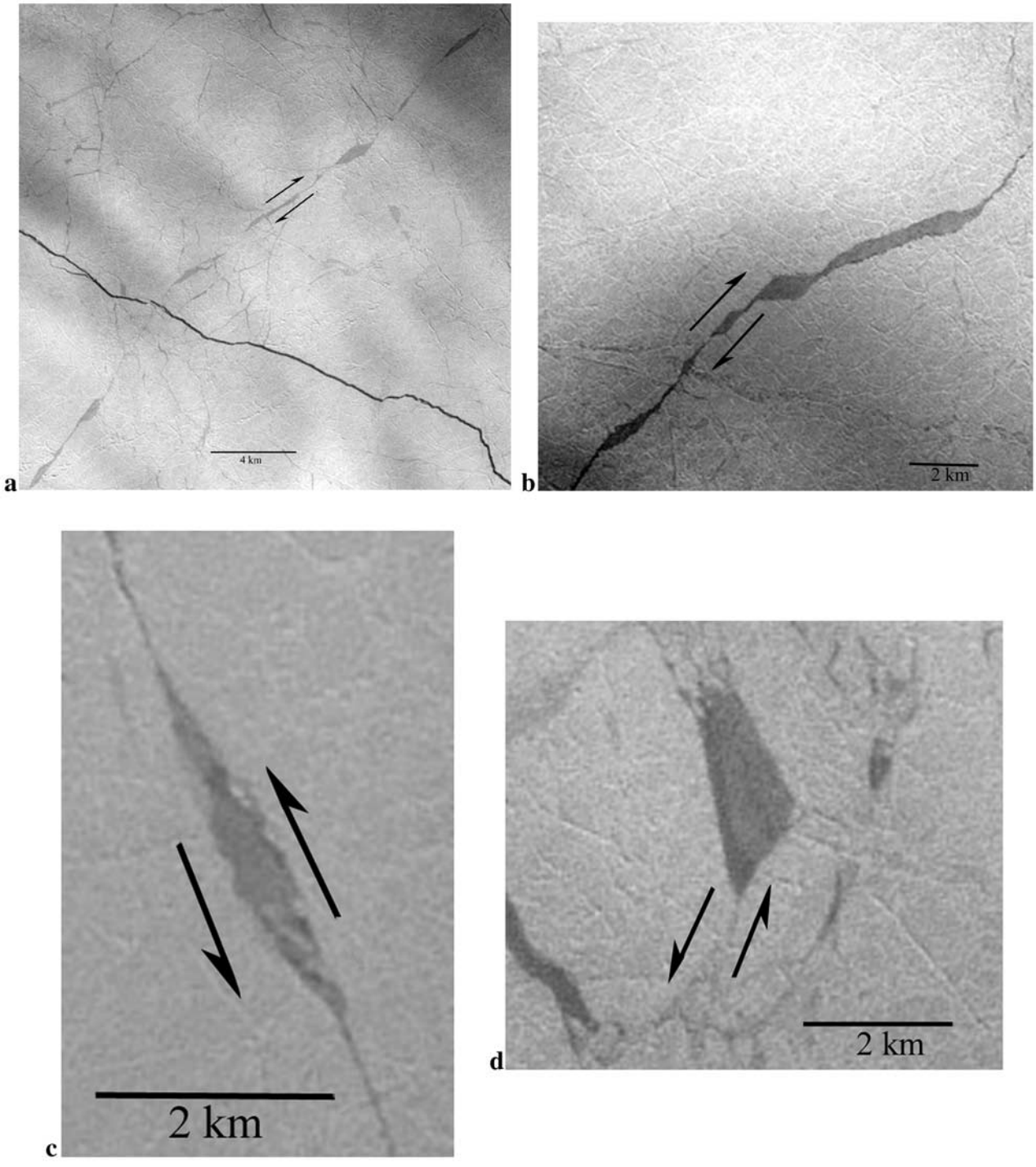

Figure 2. (a) Set of rhomboidal openings on lineament L1 of Figure 1. No rhomboid detected. North is up. Set of rhomboidal openings on lineament (b) L3, (c) L4, (d) L5, (e) (L6), (f) L7, (g) L8, (h), L9, (i) L11, (j) L12, (k) L13, (l) L14, (m) L15 of Figure 1. North is up. Note the variations in contrast within the rhomboids on L4–L15, indicative of episodic sliding.

R-L set, and L-L displacement is evident along L9 and L11 (Figures 2h and 2i), which intersect the first L-L set at an angle $2\theta^\circ \sim 50^\circ$ to 60°. The sliding appears to have occurred episodically judging from the variation in contrast within most of the rhomboids (Figure 2). The first set of R-L and L-L lineaments intersect each other at an average acute angle of $2\theta = 38^\circ \pm 5^\circ$ (Table 1). The intersections are reminiscent of those seen in Advanced Very High Resolution Radar-Infrared (AVHRR-IR) satellite images of the ice cover on the Beaufort Sea during earlier winters [*Walter and*

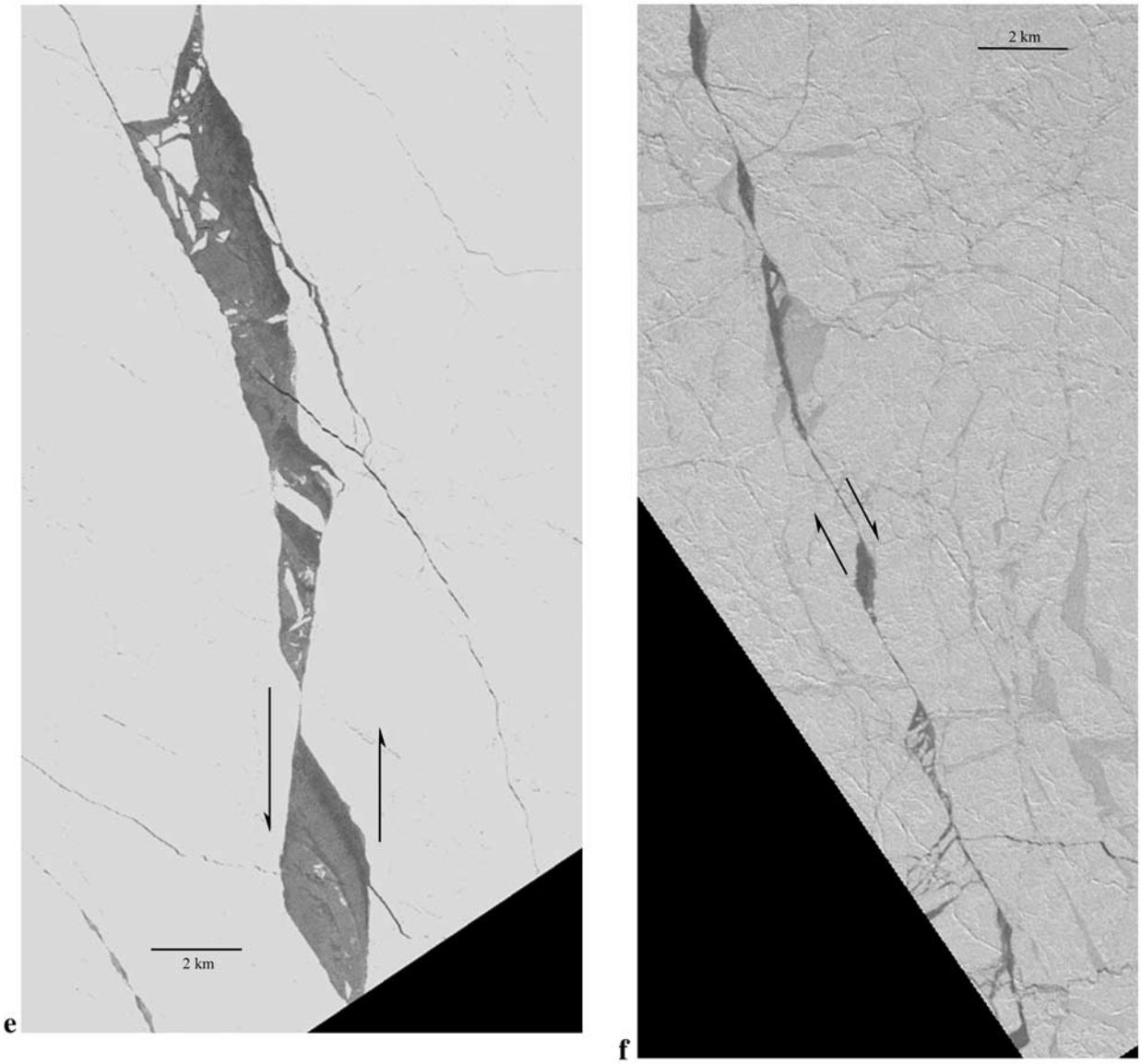

Figure 2. (continued)

Overland, 1993; *Walter et al.*, 1995; *Overland et al.*, 1995] and in RADARSAT Geophysical Processor System (RGPS) data of ice sheet deformation within the Arctic Basin during the winters of 1996–1997 and 1997–1998 [*Kwok*, 2001].

[6] The other features to note are short, secondary lineaments. One kind stems from both tips of a parent crack and is termed a wing crack, like the one first reported by *Schulson and Hibler* [1991]. Figure 4a shows an example, from near the southern tip L5. The wings are approximately oriented in a N–S direction and appear to have formed as a result of the L-L sliding along the parent lineament. Figure 4b shows another example, from near the midpoint of L8. Again, the wings are oriented approximately in a N–S direction. In this case they appear to have formed as the result of the R-L sliding along the parent crack. Theory holds [*Brace and Bombolakis*, 1963; *Nemat-Nasser and Horii*, 1982; *Ashby and Hallam*, 1986] that wing cracks form under far-field compression and then lengthen along the direction of maximum compressive stress to relax localized tensile stresses that develop on opposite sides of the tips of a parent crack as it slides, as sketched in Figure 4c.

[7] The other kind of secondary lineament is a feature that stems from one side of a parent crack. Figure 4d shows an example, from L4 just above its intersection with L6. The cracks are again oriented mainly in a N–S direction. In this instance, the secondaries form a set that creates in effect a series of slender columns, fixed on one end and free on the other (Figure 4f). We imagine that under frictional drag across the free end, the columns bend and break, like the teeth in a comb under a sliding thumb. Such sets we term comb cracks. Figures 4e shows two other examples of off-the-side secondary cracks (circled) oriented approximately in a WNW–ESE direction, from L11 from near its northern terminus and from about midway along it. This kind of

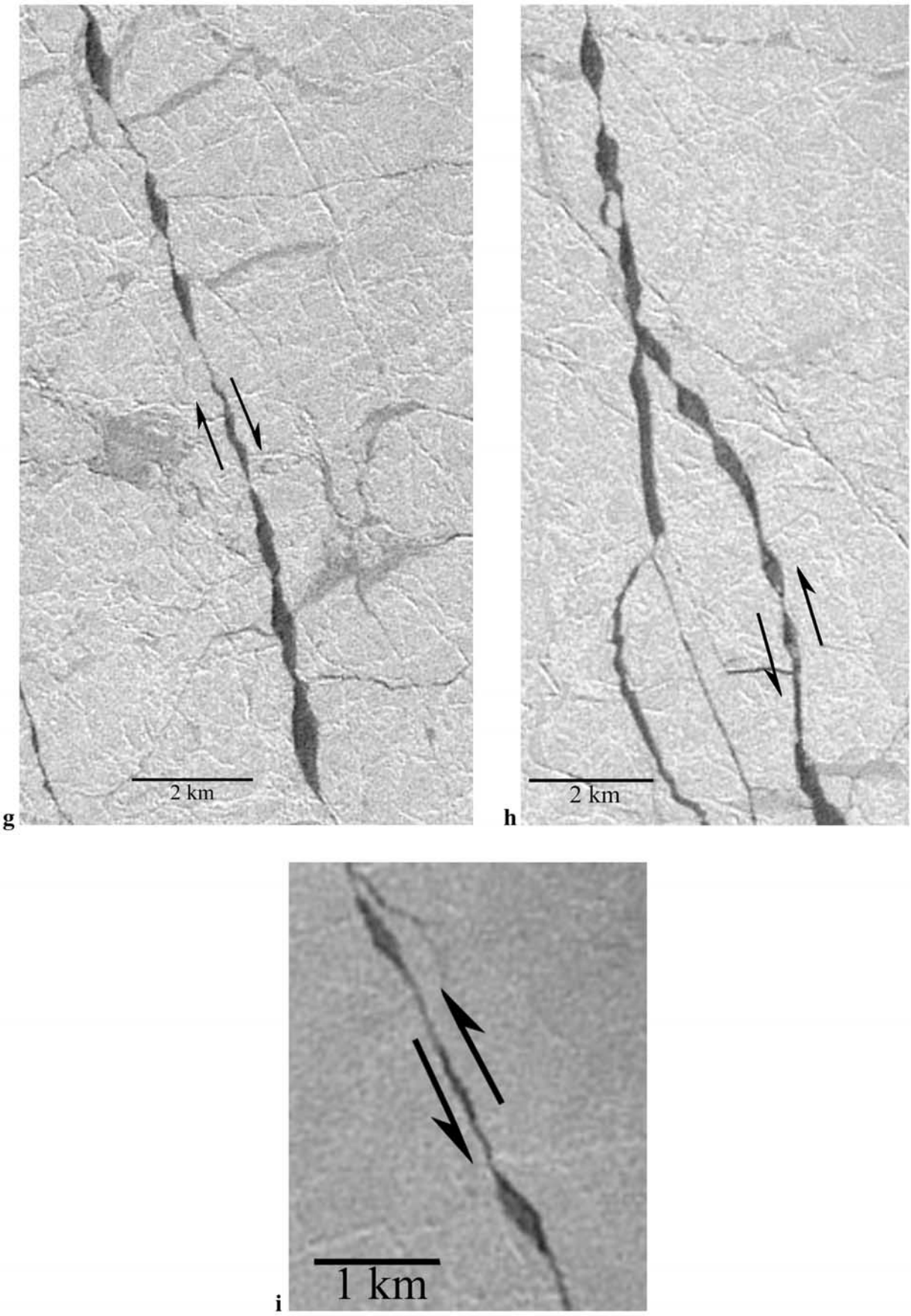

Figure 2. (continued)

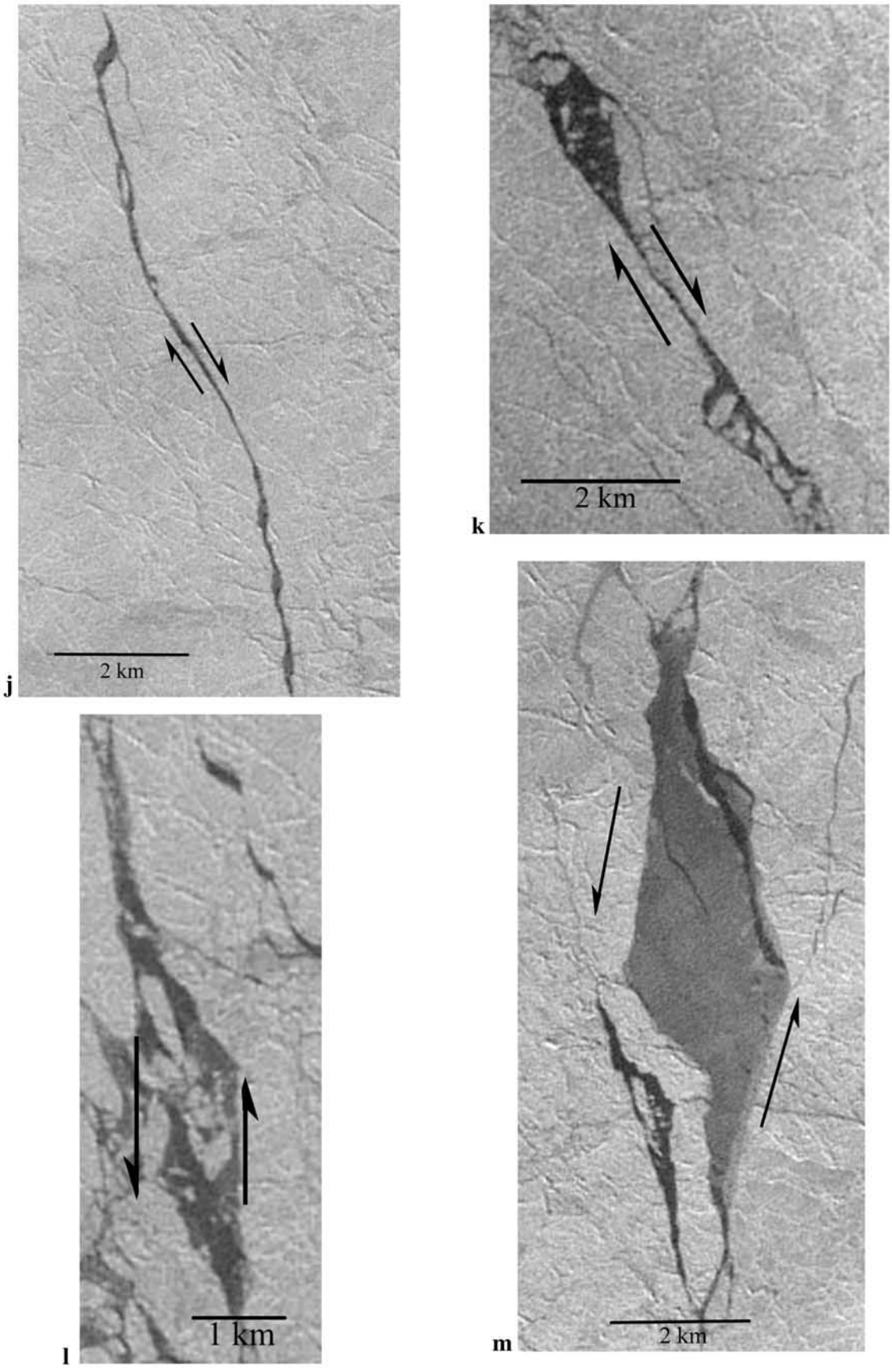

Figure 2. (continued)

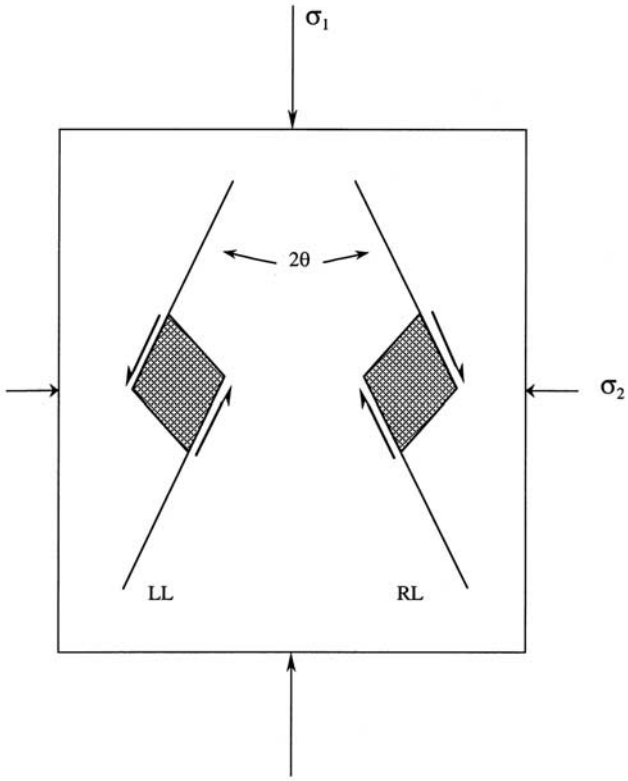

Figure 3. Schematic sketch of rhomboidal openings, showing right-lateral (R-L) and left-lateral (L-L) displacements along the attendant conjugate lineaments. The lineaments intersect in an acute angle 2θ, and are oriented with respect to the axes of principal stress as shown.

secondary crack also forms under far-field compression and aligns with the maximum compressive stress to relax localized tensile stresses [*Cooke*, 1997]. In this case, tension develops on one side of the parent crack, owing to nonuniform sliding along it [*Cooke*, 1997; *Schulson et al.*, 1999; *Renshaw and Schulson*, 2001].

2.2. RADARSAT Images

[8] To determine whether the ice sheet was deforming at the time the Landsat-7 image was obtained, we examined a time series of three synthetic aperture radar (SAR) images provided by R. Kwok (personal communication, 2003) of

Table 1. Angles of Intersection, 2θ, of Right-Lateral (R-L) and Left-Lateral (L-L) Lineaments Shown in Figure 1

Lineaments		2θ,
R-L	L-L	deg
L4	L5	45–50
L4	L6	40–45[a]
L12	L6	30–35
L13	L6	35–40
L12	L14	30–35[b]
L8	L6	35–40[c]

[a]Here 2θ is greater by ~5° near the actual intersection point.
[b]L14 exhibits along its southern section two fracture zones. We arbitrarily measured the angle between the more easterly zone and L12.
[c]Angle was obtained by extrapolating L6 and L8.

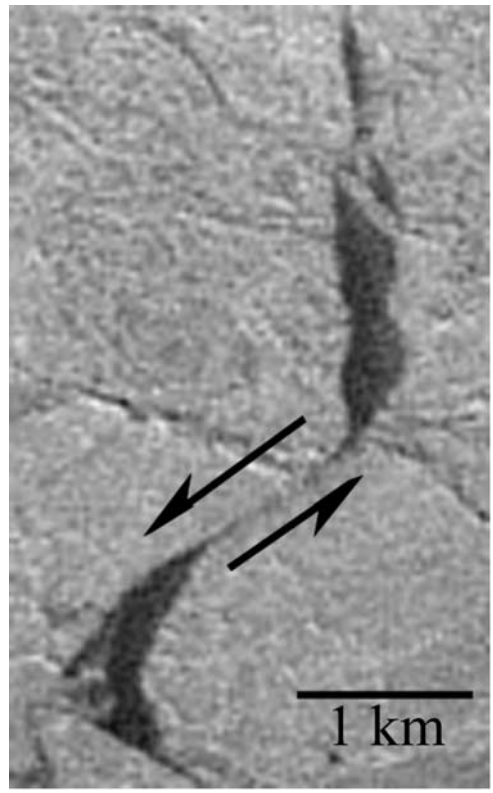

Figure 4a. Secondary cracks within the Landsat-7 scene of Figure 1. North is up. L-L wing crack on L5.

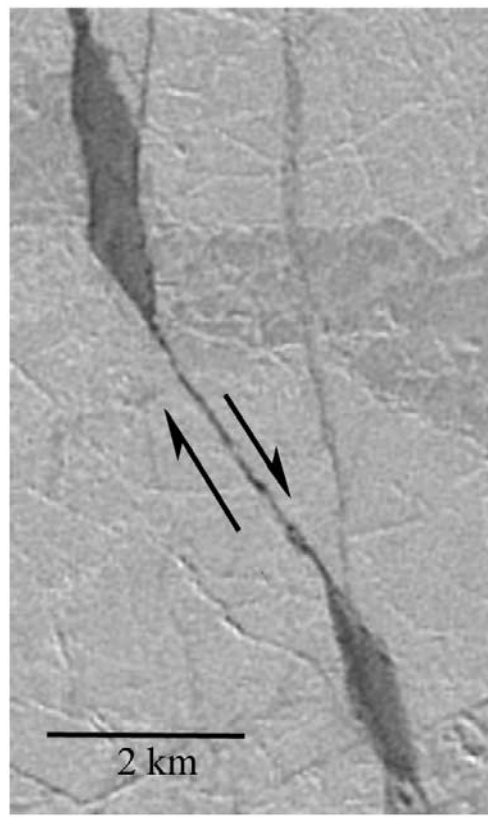

Figure 4b. Secondary cracks within the Landsat-7 scene of Figure 1. North is up. R-L wing crack on L8.

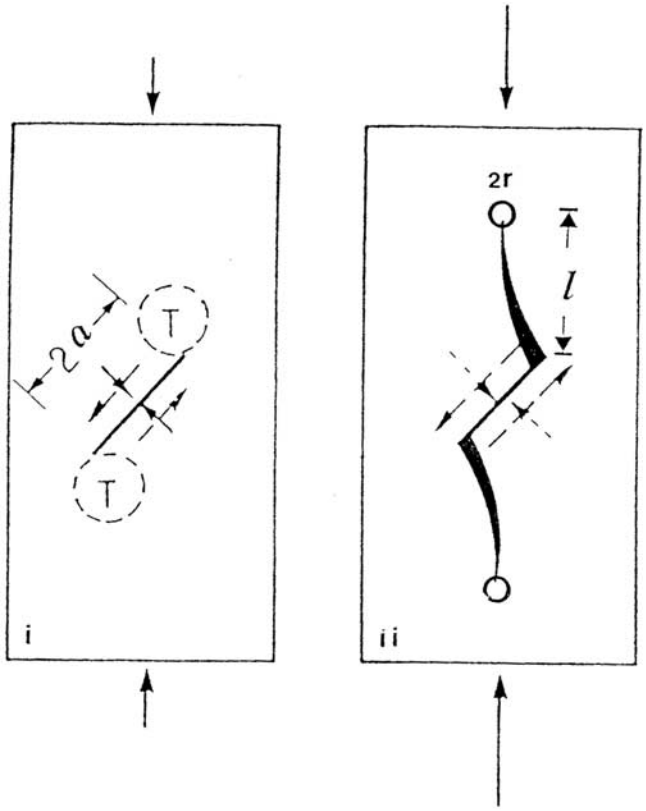

Figure 4c. Schematic sketch of a wing crack showing the development of out-of-plane extensions (ii) within the tensile (T) stress field (i) of a primary crack through L-L sliding along it.

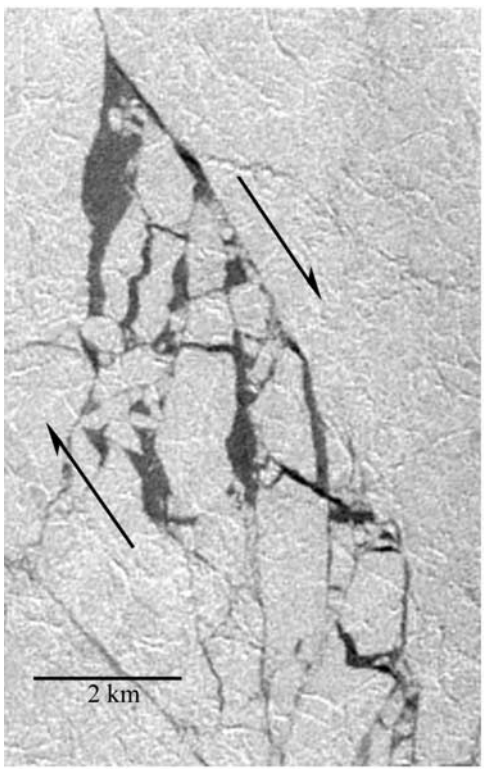

Figure 4d. Secondary or comb cracks on lineament L4 of Figure 1. North is up.

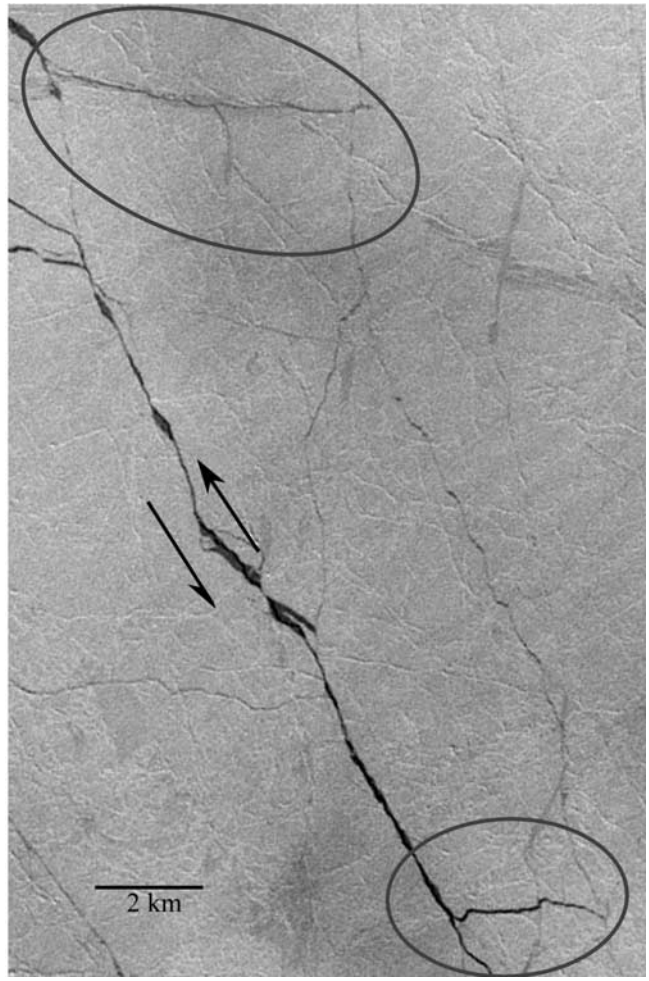

Figure 4e. Secondary cracks (circled) for lineament L11 of Figure 1. North is up.

Jet Propulsion Laboratory. The images were obtained by the Canadian RADARSAT satellite and distinguish first-year ice (darker) from multiyear ice (brighter). The three SAR images were obtained on days 81, 84, and 86 of 2000; the Landsat-7 image was obtained on day 85. Figure 5a shows the SAR image from day 84, and Figure 5b shows the corresponding part of the Landsat-7 image. (For ease of comparison, common features are labeled A, B, and C.) The SAR image does not resolve the narrow lineaments. However, it clearly resolves the rhomboidal-shaped openings on L4, L6, and L15. In fact, it resolved those features on day 81, implying that most of the sliding that created them had occurred at least 4 days before the Landsat image was obtained. When animated, the time series reveals some relative movement and rotation, albeit subtle and thus difficult to communicate. With R. Kwok's permission, we posted his animation on the following web site: www.thayer.dartmouth.edu/~icelab; it may be viewed by clicking on "SAR movie." It shows, for instance, that from day 81 to 84 the cover rotated slightly in a clockwise sense, opened by about 0.2 km along the trace of L10 (that we mentally superimposed on the animation), and slid by a similar amount in a L-L sense along the traces of L4 and L11. Note that the L-L displacement along L4 is opposite to the

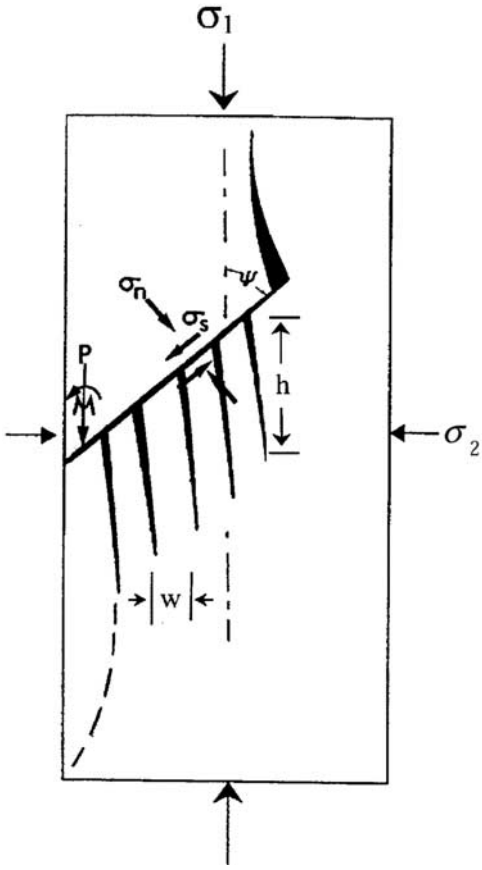

Figure 4f. Schematic sketch of a comb crack [from *Schulson et al.*, 1999]. Secondaries form on one side of a primary crack, creating fixed-free slender microcolumns loaded mainly by frictional drag across the free ends.

R-L movement assigned above (section 2.1), suggesting that the direction of sliding changed over the history of the feature. We detected no relative movement along L6, L12, L14, and L15. The SAR field does not include the region of the eight other Landsat-7 lineaments, and so we do not know whether the ice was deforming there.

[9] It appears, therefore, that although a few lineaments within the Landsat scene were moderately active at the time the image was obtained, most were essentially inactive. This implies that the deformation that created them had occurred at least several days earlier. The inactivity implies also that some post-deformation healing probably occurred.

2.3. Observations From a Twin Otter

[10] The features observed on the Landsat-7 image ranged in size from about 100 km to 0.1 km. To determine whether sliding lineaments and other features form on a smaller scale, we viewed part of the arctic sea ice cover during winter 2003 from a Twin Otter aircraft. During the 5-day period 6–10 April 2003, we made observations from altitudes of 150 m to 2900 m, between Prudhoe Bay, Alaska (70°N, 148°W) and Ice Camp ICEX03. The camp was provided by the Office of Naval Research, and was initially located at 73°N, 148°W. The cover along the flight path was composed largely of first-year ice, according to analyses by the National Ice Center, and its thickness at the camp was 1.8 m. We flew at a speed of 240 km/hr (67 m/s). For the most part, the weather was clear. We photographed the icescape using digital, 35-mm, and video cameras, and (for most images) noted the camera angle, the focal length, and (from a hand-held GPS device) the latitude/longitude coordinates.

[11] We observed both open and closed lineaments. The open ones often appeared as members of multistranded, subparallel, discontinuous sets that generally exhibited either R-L or L-L relative displacement, marked by rhomboidal-shaped openings. As in the Landsat-7 scene, the rhomboids exhibited variations in contrast, again indicative of episodic sliding. We also observed wing cracks that had been created by either R-L or L-L sliding, and we observed a comb crack. For instance, Figure 6a shows an open L-L lineament as well as a pressure ridge; Figure 6b shows a wing crack plus an attendant shear ridge that appear to have formed as a result of R-L sliding along the parent crack; and Figure 6c shows a comb crack that formed along a closed L-L lineament, owing presumably to nonuniform sliding.

[12] Although of a different time and place from the Landsat-7 scene, the Twin Otter observations show that sliding lineaments and secondary cracks also form on the meter scale, i.e., on the scale of the ice thickness. Their strand-like and discontinuous character suggests that major lineaments of the kind detected by Landsat-7 are also probably composed of through-thickness bands of damage.

2.4. Observations From the Laboratory

[13] To determine whether similar fracture features also form on the submeter scale, we performed biaxial compression experiments in the laboratory. We made specimens from ice of two different origins, but with essentially the same columnar fabric and S2 crystallographic texture (defined below) that characterizes first-year sea ice. One set of specimens originated in the laboratory, from ice we grew there by unidirectionally freezing Hanover tap water, following established procedures [see *Schulson and Nickolayev*, 1995]. The other originated in the field, from a 112-kg block that we harvested from the first-year sea ice cover at the ICEX03 camp described above (section 2.3). The average column diameter for each material was ~6 mm, and the crystallographic c-axes were confined more or less to the horizontal plane of the parent ice covers, but were randomly oriented within this plane, giving the so-called S2 structure [after *Michel and Ramseier*, 1971]. The salinity of the sea ice was ~7 ppt and was obtained from meltwater measurements of electrical conductivity using known standards. We prepared plate-shaped specimens of dimensions 152 mm × 152 mm × 25 mm in thickness in which the long axes of the columnar-shaped grains were perpendicular to the largest faces, and then loaded them in directions perpendicular to the columns to simulate the natural loading of a floating ice sheet. Before loading, the ice was equilibrated to a temperature of −10°C. The specimens were deformed at a strain rate (along the major axis) of $3-5 \times 10^{-3}$ s^{-1} using a rigid, multiaxial, servo-hydraulic loading system housed within a cold room in Dartmouth's Ice Research Laboratory. Details will be given elsewhere. Here we focus on the main failure features.

[14] Figure 7a shows a set of four subparallel narrow lineaments or faults (see pointers) that formed very near terminal failure within a specimen of the first-year sea ice. The specimen was deformed by proportionally loading along

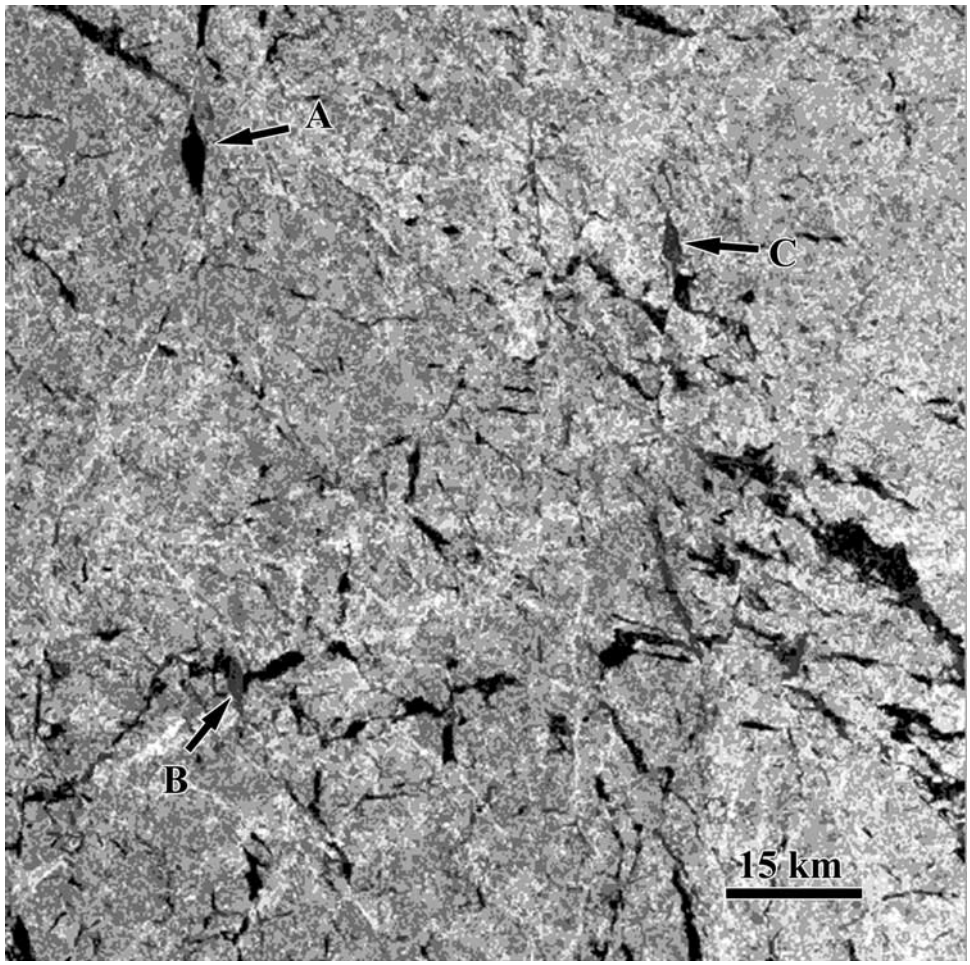

Figure 5a. RADARSAT image. Letters A, B, and C correspond to the large rhomboids on lineaments L4, L6, and L15, respectively, of Figure 1. North is up. The image was obtained on day 84 of 2000, or 24 March 2000, and was provided by R. Kwok of Jet Propulsion Laboratory (©CSA 2002).

the path $R = \sigma_2/\sigma_1 = 0.1$ such that the minor stress, σ_2, was a constant fraction of the major stress, σ_1, during the experiment. Terminal failure occurred when the maximum principal stress (taken in this paper as the most compressive stress) reached $\sigma_{1f} = 10.1$ MPa. The features are oriented about 25°–30° to the direction of σ_1. The faults constitute localized, mechanical instabilities whose formation led to a sudden and large drop in load and to the termination of the test. Prior to termination, short secondary cracks developed as well, as the load increased beyond about one third of the terminal strength. The cracking was accompanied by small load drops.

[15] Figure 7b shows another set of lineaments/faults, similarly oriented with respect to σ_1. This set formed within freshwater ice when loaded and brought to terminal failure under the same stress state, temperature and strain rate. The failure stress was $\sigma_{1f} = 10.2$ MPa, i.e., essentially the same as that of the sea ice. In this example, conjugate sets formed, analogous to the intersecting lineaments within the sea ice cover (Figure 1 and Table 1). The intersection angle, however, was generally larger than in the ice sheet ($2\theta = 50°–55°$ versus $38° \pm 5°$), but typical of failure in the laboratory at −10°C [*Iliescu and Schulson*, 2004]. Conjugate faulting developed in the specimens of sea ice as well. However, in both kinds of material, failure along conjugate sets was less common than single-set faulting. Detailed examination of the freshwater ice, reported earlier, revealed that the small-scale faults were composed of deformation-induced wing cracks and comb cracks [e.g., see *Schulson et al.*, 1999, Figure 2] (for review see *Schulson* [2001]) and that the secondary cracks, once they had lengthened somewhat, were oriented in a direction essentially parallel to σ_1, as theory dictates [*Brace and Bombolakis*, 1963; *Nemat-Nasser and Horii*, 1982; *Ashby and Hallam*, 1986; *Cooke*, 1997; *Renshaw and Schulson*, 2001].

[16] None of the lineaments evident in Figures 7a and 7b shows rhomboidal openings. That is because the experiments were terminated just after the features developed. When post-failure deformation was imparted (after shimming the two parts of the specimen to avoid end crushing), sliding occurred and rhomboids formed, similar in appearance to the larger ones in the sea ice cover. For instance, Figure 7c shows an example along another lineament after a R-L displacement of 10 mm had been imposed. We thus found, on the millimeter-to-centimeter scale, features that were similar in appearance to the ones we found on the two larger scales.

2.5. Comment

[17] What does this "look-alikeness" mean? One response is that it is simply fortuitous and thus meaningless.

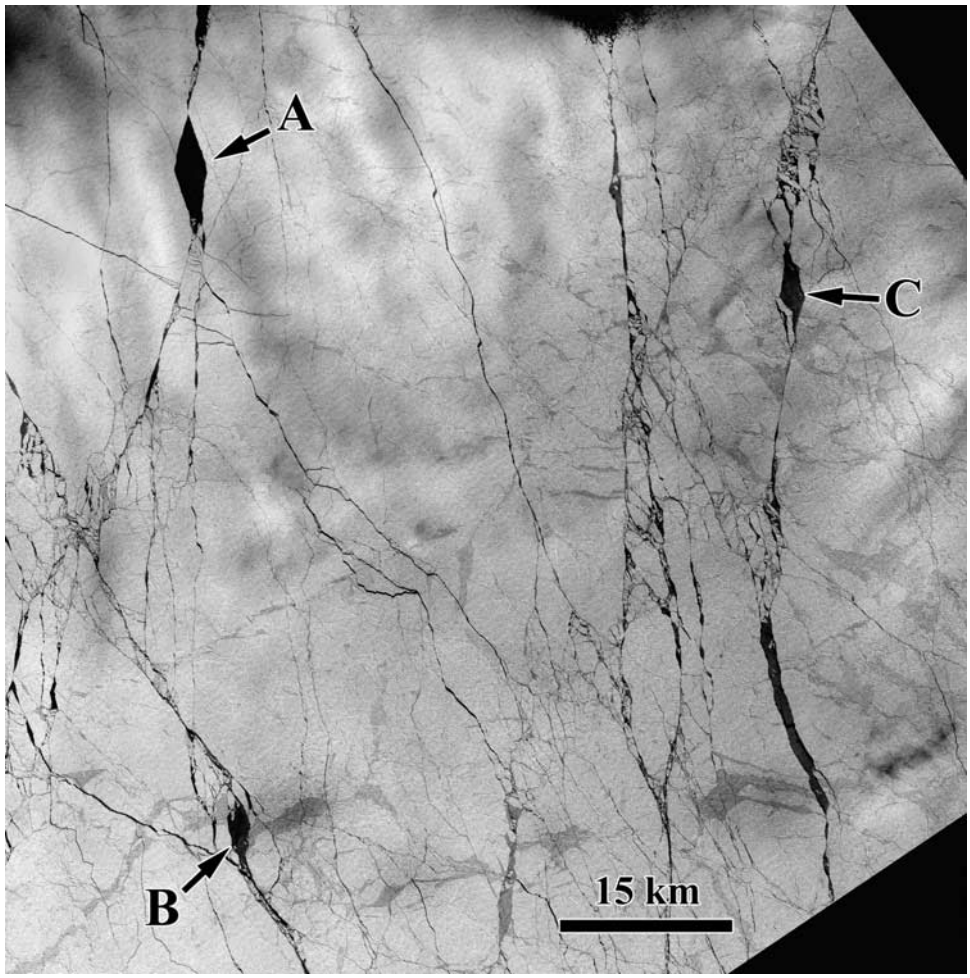

Figure 5b. Landsat-7 image corresponding to the RADARSAT image of Figure 5a. Letters A, B, and C are the same as in Figure 5a.

On the other hand, when coupled with the similarity that *Erlingsson*'s [1988, 1991] noted when examining arctic leads (100–1 km) and with the similarity that *Rothrock and Thorndike* [1984], *Weiss and Gay* [1998], and *Weiss* [2001] observed when examining ice floes (RT: 30–0.1 km) and compressive fracture fragments (W: 50–0.1 mm), respectively, a similarity in the latter two instances that generated a similar fractal dimension (D_{RT} = 2.0 ± 0.2; D_W = 2.09 ± 0.15), we are inclined to be less dismissive. Instead, the similarity in appearance may indicate that a floating ice sheet, although intrinsically more complicated than a laboratory specimen and stressed more heterogeneously, deforms through the same basic process as the smaller body. In other words, fracture physics may be scale independent and, in keeping with recent strain rate analysis (D. Marsan et al., Scale dependence and localization of the deformation of arctic sea ice, submitted to *Physical Review Letters*, 2004) (hereinafter referred to as Marsan et al., submitted manuscript, 2004), deformation on many scales may contribute to the deformation of the winter sea ice cover.

[18] We are aware that the concept of scale-independent fracture physics may be controversial. *McNutt and Overland* [2003], for instance, express the view that different physics may be operating at different scales, citing as evidence *Sanderson*'s [1988] report that the failure stress of a sea ice sheet appears to be about a factor of 10^3 lower than that of a laboratory specimen. They [*Overland et al.*, 1995; *McNutt and Overland*, 2003] then invoke hierarchy theory of complexity (for a review, see *O'Neill et al.* [1986]) and argue that it is the degree of disconnectedness between scales that accounts for the organization of the system. In so doing, they emphasize the idea of an emergent property that represents a discontinuity in scale "where the whole is greater than the sum of the parts." A transition in scales is specified as somewhere between the "multifloe scale" of 2–10 km and the "aggregate scale" of 10–75 km [*McNutt and Overland*, 2003]. A problem with the hierarchy approach applied to the ice cover is that the different scales (e.g., floe scale <1 km; multifloe scale 2–10 km, and so on) seem to be defined rather arbitrarily. More importantly, the approach seems to contradict the results of fractal analyses, which reveal neither a characteristic length in the fragmentation pattern of ice in nine orders of magnitude [*Weiss*, 2003], from 10^{-4} m to 10^5 m, which includes the proposed transition scale, nor a characteristic length in the deformation rate of the winter sea ice cover over the range 10 km to 1000 km (Marsan et al., submitted manuscript, 2004). In fact, the latter study shows

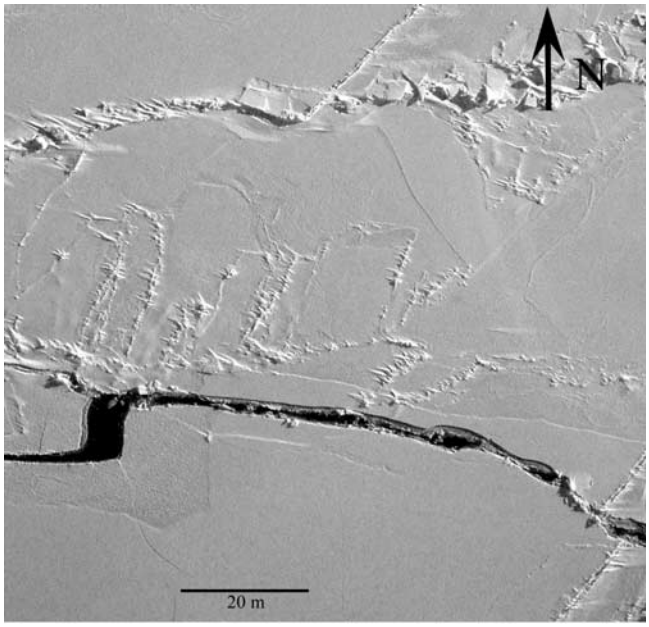

Figure 6a. Aerial photograph of the ice cover on the Beaufort Sea showing an open lineament characterized by left-lateral relative movement. Note the finger rafts and the offset of the ridge located near the eastern end of the open lineament. Date is 10 April 2003. Coordinates are 72.17°N/148.37°W. This is a digital image with the camera vertical.

that the average deformation rate increases slightly with decreasing scale, and that the distribution in rate at a given scale increases strongly with decreasing size, to the point that most of the deformation may actually be occurring on the smaller scale (Marsan et al., submitted manuscript, 2004). As to the difference in strength, that observation could be accounted for in terms of the difference in size of stress concentrators; i.e., $\sigma_{lab}/\sigma_{field} = (a_{field}/a_{lab})^{0.5} = (\text{kilometer/millimeter})^{0.5} = 10^3$. The difference might also be accounted for in terms of the limited temporal resolution of in situ stress measurements (e.g., 5 min in the work by *Richter-Menge and Elder* [1998]; 1 hour in the work of *Richter-Menge et al.* [2002]) and in the possibility that very short-term, higher-stress events were not recorded in the field data. We thus retain the concept of scale independence and examine it more quantitatively below.

3. Interpretation and Analysis

3.1. Sliding Lineaments Within the Sea Ice Cover

[19] Returning to the lineaments and to the secondary cracks detected by Landsat-7, we propose that these features formed under a far-field stress state of biaxial compression characterized by moderate confinement. (We specify moderate confinement for the reason given in section 5.) This view reflects not only the similarity in appearance to the small-scale compressive features, but also the predominant character of the stress state that appears to develop annually within the ice cover during winter, judging from in situ measurements by *Richter-Menge and Elder* [1998] and by *Richter-Menge et al.* [2002]. Those measurements show that the dominant stress state is compressive, characterized by a moderate degree of confinement, and that it originates in relative motion of (i.e., velocity gradients within) the cover. The divergence that is evident from the Landsat image does not necessarily contradict the assignment of compressive failure, because, as concluded from the RADARSAT study (section 2.2), the events that created the lineaments essentially ended before the image was obtained, allowing time for the cover to open up under ocean currents and/or changes in wind stress.

[20] More specifically, we interpret the subparallel R-L lineaments L4, L7, L8, L12, and L13 and the subparallel L-L lineaments L5, L6, L14, and L15 of Figure 1 to be members of a conjugate set of compressive features whose formation marked the culmination of a major wind-driven event during which the direction of maximum principal stress was oriented approximately in a N–S direction. The secondary cracks that were oriented in this direction (Figures 4a, 4b, and 4d) probably formed during the same event. We interpret the other R-L lineaments (L1 and L3) and the other L-L lineaments (L9 and L11) to be compressive features that probably formed during a second event, on conjugate planes for which the principal stress was oriented roughly WNW–ESE. Left-lateral sliding along L4 appears to have occurred during this second event, as already noted from the RADARSAT images (section 2.2). The off-the-side secondary cracks that were oriented in the WNW–ESE direction (Figure 4f) probably formed during this second event as well. The large and somewhat distorted rhomboid along L4 (Figure 1) can then be viewed as having formed first through R-L sliding under the proposed N–S principal stress and then modified through L-L sliding under the proposed WNW–ESE principal stress. In other words, and in keeping with an assignment by *Marko and Thomson* [1977] following an earlier examination, the sliding lineaments appear to be analogous to strike-slip faults within Earth's crust [see *Jaeger and Cook*, 1979; *Sylvester*, 1988; *Scholz*, 1990]. For this reason, we term them compressive shear faults, or more specifically still, "brittle" compressive shear faults to distinguish them from nondilatant "ductile" compressive shear faults. The latter kind of fault forms when ice is rapidly loaded under high degrees of triaxial confinement (and thus is probably not important in sea ice covers), is oriented on planes inclined by ~45° to the direction of maximum principal stress, is accompanied by little or no cracking, and results, we think, from adiabatic heating through dislocation slip along localized shear bands [*Schulson*, 2002a].

[21] This leaves L2 and L10. As already mentioned, we detected no evidence of relative shear movement along these lineaments. Perhaps they formed either under a different stress state or under a higher degree of biaxial confinement in the manner of a thrust fault within Earth's crust (more in section 5).

[22] It could be argued that in interpreting the Landsat lineaments as compressive shear faults, we are violating a fundamental tenet of fracture mechanics, namely, that the macroscopic plane of faulting be parallel to the direction of the intermediate principal stress [*Rudnicki and Rice*, 1975; *Jaeger and Cook*, 1979], which lies within the plane of the sheet. However, that requirement is based upon isotropic mechanical behavior. Sea ice is mechanically anisotropic. Owing to its S2 growth texture described above and to thermal cracks and other stress concentrators, material of an

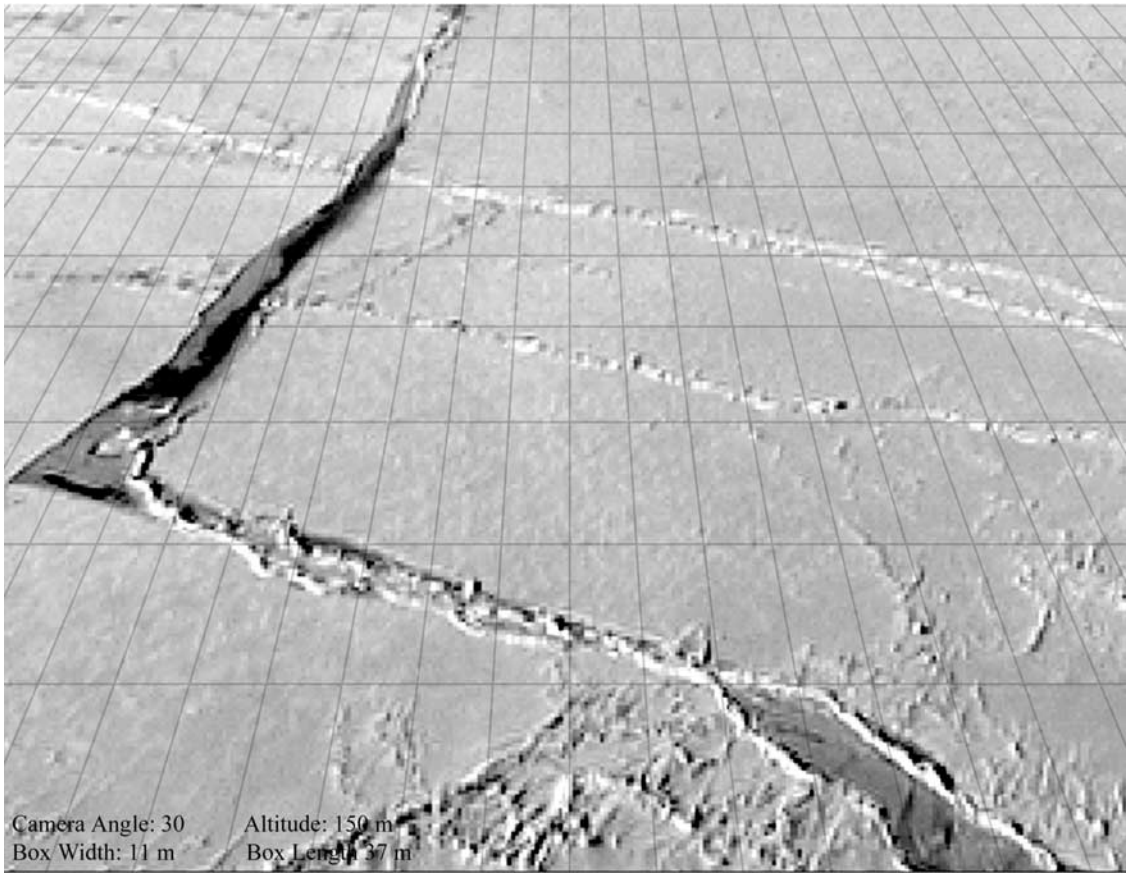

Figure 6b. Aerial photograph of the ice cover on the Beaufort Sea showing a wing crack that formed as the result of right-lateral relative movement along a parent lineament. Note the contrast within the wing extension, indicative of episodic sliding. Also note the shear ridge along the parent crack. Date is 8 April 2003. Coordinates are about 71.5°N/148°W. This is a video image with the camera angle 30° off horizontal Box width is 11 m; box length is 37 m. North is horizontal and points to the right.

ice sheet is several times stronger in the through-thickness direction than in directions within the horizontal plane [*Dykins*, 1970; *Kuehn et al.*, 1990]. This means that under a low degree of biaxial confinement, inelastic displacement in the through-thickness direction is suppressed. Thus our interpretation does not violate a fundamental tenet of brittle compressive failure.

[23] It might be argued also that the larger-scale fracture features developed not under biaxial compression, but under combined compressive and tensile loading, in recognition of

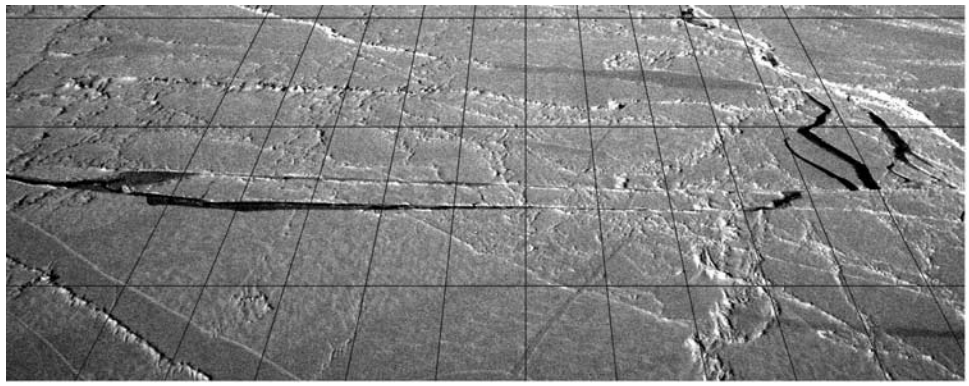

Figure 6c. Aerial photograph of the ice cover on the Beaufort Sea showing a comb-like crack stemming from one side (near the right-hand terminus) of a left-lateral lineament. Note the rhomboid along the lineament. Date is 8 April 2003. Coordinates are 71.36°N/148.32°W. This is a digital image with camera angle 30° off horizontal. Box width is 40 m; box length is 160 m. North is horizontal and points to the right.

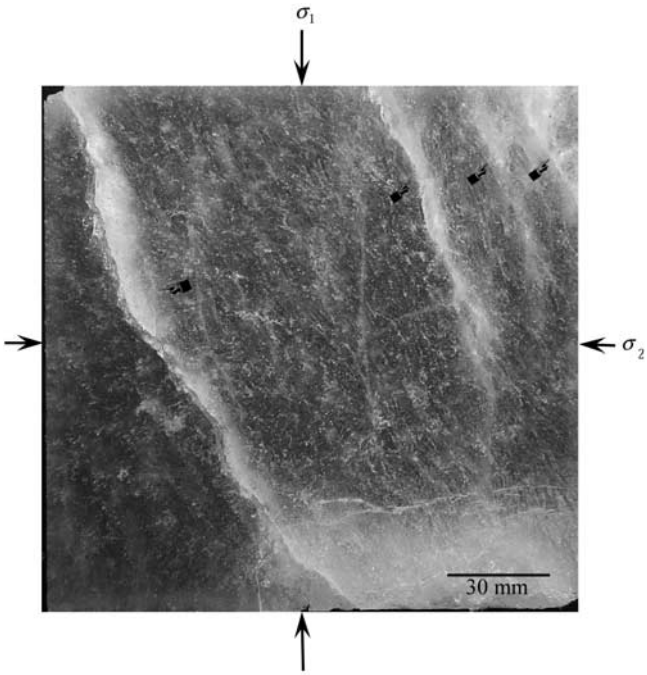

Figure 7a. Photograph of a specimen of first-year columnar S2 sea ice biaxially loaded across the columns to terminal failure at −10°C. The columnar grains run in and out of the plane. The image shows a set of four shear faults (see pointers) inclined by 25°–30° to the direction of maximum principal stress, σ_1.

an interpretation by *Muehlberger* [1961] of small-angle conjugate fractures in rock. However, from our experience on the brittle failure of ice in the laboratory (for a review, see *Schulson* [2001]), this possibility seems unlikely. Under an applied tensile stress, brittle fracture of both saltwater and freshwater ice always occurs on a single macroscopic fracture plane oriented perpendicular to the direction of loading, not on a set of subparallel planes distributed throughout the volume of the material. Under uniaxial compression (when care is taken to reduce lateral stresses at the boundaries through the use of laterally compliant loading platens) the materials fracture along subparallel sets of macroscopic planes aligned with the direction of loading, not unlike the ice sheet breakouts *Overland et al.* [1998] observed and attributed to compressive loading. We would expect, therefore, that under combined tension and compression applied orthogonal to each other, ice would fracture along a plane perpendicular to the tensile direction and parallel to the compressive direction, and not along conjugate planes as seen here.

[24] Finally, in view of the extreme slenderness of a first-year sea ice sheet (of typical thickness 1.8 m to 2.8 m [*Laxon et al.*, 2003] compared with an effective "length" of the order of 10^3 km or greater), it could be argued that processes which operate within what is often viewed as a two-dimensional (2-D) body probably differ from those which operate within a 3-D body. For instance, elastic buckling might seem to be a more likely compressive failure mode. On that point, calculations (Appendix A) indicate that the expected buckling stress (10–12 MPa) is more than a factor of 40 higher than the highest stresses that *Richter-Menge and Elder* [1998] and *Richter-Menge et al.* [2002] have measured in situ. Similarly, thermal cracking might seem to be a more likely mode of failure than compressive shear faulting, for long lineaments of that origin are known to develop within the sea ice cover [*Evans and Untersteiner*, 1971; M. D. Coon, personal communication, 2003]. The problem with that interpretation is that it cannot account for the organization of the fracture pattern: Thermal cracks are expected to be more randomly oriented than the features described here. The other point worth noting concerns thickness, per se. Although it is impossible in the laboratory to reproduce S2 ice with the same slenderness ratio as a floating ice sheet, we have varied the along-column thickness of our specimens, from ~10 mm to 152 mm, thereby changing the slenderness ratio by an order of magnitude or so, from 0.06 to unity. In so doing, we detected no significant effect on either the biaxial failure strength or the failure mode. While those ratios are still very large relative to an ice sheet, the absence of an effect of thickness is at least consistent with the hypothesis that the same processes may govern the failure of a floating sea ice sheet and a specimen from the sheet.

3.2. Intersection Angle

[25] Consider next the intersection angle for conjugate faults. Since localized failure is governed by a Coulombic-

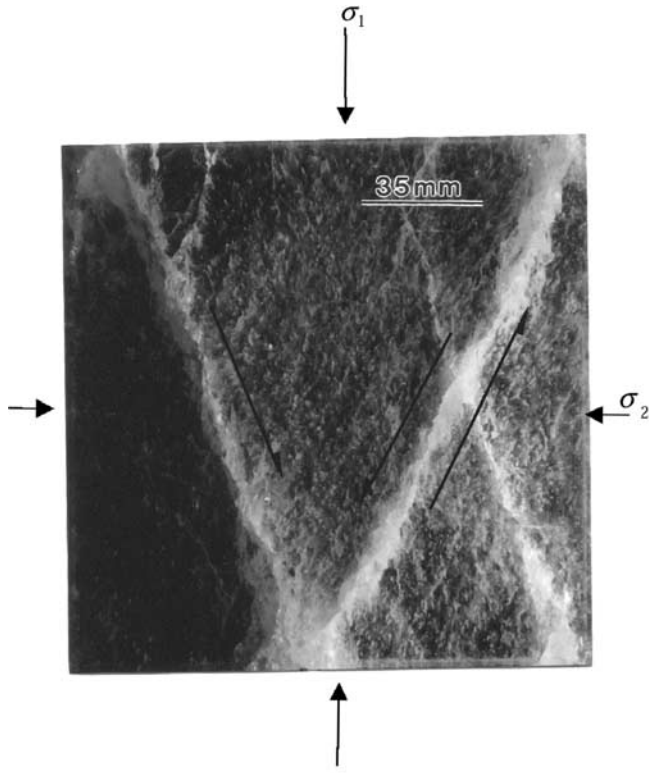

Figure 7b. Photograph of a specimen of columnar S2 freshwater ice biaxially loaded across the columns to terminal failure at −10°C. The columnar grains run in and out of the plane of the paper. The image shows a conjugate set of brittle compressive shear faults oriented at ~30° to the direction of maximum principal stress, σ_1.

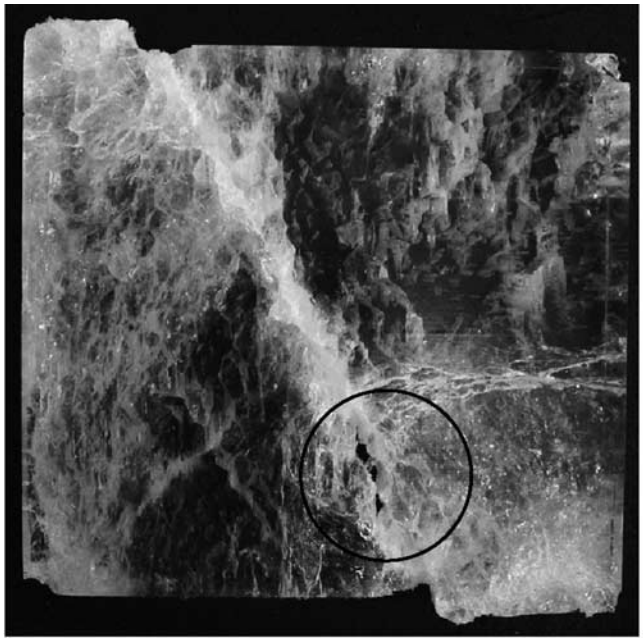

Figure 7c. Photograph showing a specimen of columnar S2 freshwater ice biaxially loaded across the columns to terminal failure at −10°C. The columns run in and out of the plane of the paper. The image shows a right-lateral compressive shear fault and a rhomboidal opening (circled) along it that was created by sliding 10 mm over the fault. Width is 150 mm.

type criterion both in the field [*Erlingsson*, 1988; *Overland et al.*, 1998; *Coon et al.*, 1998] and in the laboratory [*Schulson and Nickolayev*, 1995], the intersection angle, 2θ, or the inclination, θ, of a fault on either side of the direction of maximum principal stress can be interpreted in terms of a coefficient of internal friction, μ. Assuming that μ is independent of confinement and that the fracture zone has no width, compressive failure theory dictates [*Jaeger and Cook*, 1979; *Ashby and Hallam*, 1986]

$$\tan\ 2\theta = 1/\mu. \tag{1}$$

When the actual, finite width of the fault is considered [*Hibler and Schulson*, 2000], a composite friction coefficient emerges that leads to somewhat smaller effective internal friction as confinement increases and thus to a larger intersection angle [*Schulson and Hibler*, 2004]. However, for our purpose here and to allow comparison to an earlier analysis, we adopt the simpler approach that is embodied in equation (1). Then for the range of intersection angles noted in Table 1, the internal friction coefficient ranged from $\mu = 0.8$ (for $2\theta = 50°$) to $\mu = 1.7$ (for $2\theta = 30°$). *Marko and Thomson* [1977] deduced the value $\mu = 1.7$ to 1.9 from a similar analysis. The meaning of these values is beyond the scope of this paper. We wonder, however, whether the variation might reflect not only a possible variation in the degree of confinement, but also variable contact along the sliding fault. Sliding speed, which seems to vary from fault to fault [*Kwok*, 2001; *Moritz and Stern*, 2001], may also be a factor, and perhaps the dominant one, for experiments [*Fortt et al.*, 2003; *Fortt and Schulson*, 2004] in the laboratory on the resistance to sliding along naturally formed brittle compressive shear faults indicate that the internal friction coefficient decreases with increasing speed once the velocity is large enough (>0.1 mm/s at −10°C).

[26] Why the average intersection angle in the Landsat-7 scene is generally less than that in the laboratory ($2\theta \sim 38°$ versus $2\theta \sim 53°$) is not clear. One possible explanation is that the ice sheet on average was colder than the test specimens, i.e., colder than −10°C. We base this suggestion upon the observation [*Kennedy et al.*, 2000] that the kinetic coefficient of friction for saltwater ice sliding slowly against itself in the laboratory, although probably of somewhat different nature from the internal coefficient, increases with decreasing temperature. Differences in roughness might also be at play, for this factor also affects the friction coefficient in the laboratory [*Fortt and Schulson*, 2004]. We are planning new experiments to test some of these possibilities.

3.3. Estimate of the Maximum Principal Stress Within the Sea Ice Cover

[27] If fracture physics is truly scale independent, then one should be able to estimate within an order of magnitude the maximum principal stress, σ_1, under which field features form. With that goal in mind we applied wing-crack [*Ashby and Hallam*, 1986] and comb-crack [*Schulson et al.*, 1999; *Renshaw and Schulson*, 2001] mechanics to the secondary cracks within the Landsat-7 and Twin Otter images we described above. While the estimates we obtained pertain specifically to the creation of the secondary cracks, they may be considered also as a lower limit for compressive shear faulting.

[28] For the wing cracks shown in Figures 4a and 4b,

$$\sigma_1 = \frac{K_c\sqrt{L}}{\sqrt{\pi a}(.23(1-\mu_k))} \tag{2}$$

(for $\mu_k < 1$), where K_c is fracture toughness, a is the half-length of the parent, sliding crack, $L = l/a$ where l the length of the wing (defined in Figure 4c), and μ_κ is the kinetic coefficient of friction. Taking $\mu_\kappa \sim 0.5$ [*Kennedy et al.*, 2000] and $K_c \sim 250$ kPa $m^{0.5}$ [*Dempsey*, 1996], $a \sim 2$ km and $L \sim 2$, equation (2) gives a maximum principal stress of $\sigma_{1f} \sim 40$ kPa at failure. Similarly, for the smaller-scale wing crack shown in Figure 6b, where $a \sim 60$ m and $l \sim 200$ m, we obtain $\sigma_{1f} \sim 300$ kPa.

[29] For the comb-crack shown in Figure 4d,

$$\sigma_1 = \frac{2K_c}{\sqrt{3 \propto h}(1-\mu_k)}, \tag{3}$$

where α is the slenderness of the microcolumns and is given by the ratio of column height, h, to width, w (defined in Figure 4f). Using the same values of K_c and μ_κ and taking $\alpha = h/w \sim 2$ and $h \sim 2$ km, equation (3) gives a failure stress of $\sigma_{1f} \sim 9$ kPa.

[30] We caution that these are rough estimates. The calculations were made only for the creation of specific types of cracks and not for the process of crack interaction and linkage that precedes fault formation (more below); they ignored the strengthening effect of confinement; and

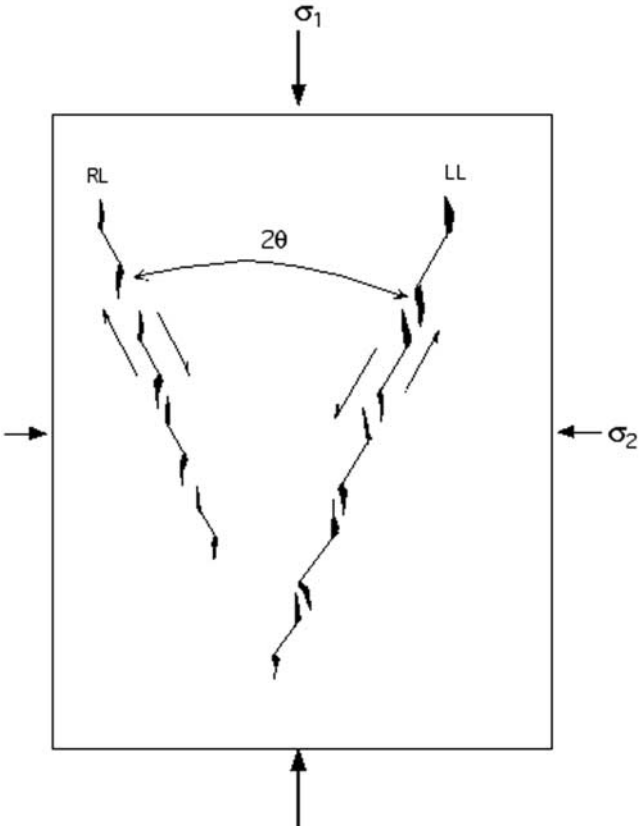

Figure 8a. Schematic sketch of proposed mechanism that triggers brittle compressive shear faulting via the linking of en echelon arrays of wing cracks.

they employed values of the materials parameters that may differ from the actual values applicable under field conditions. Also, no account was taken of possible effects of deformation damage (on a scale too fine to be resolved by Landsat-7) on the fracture toughness of the ice cover. Nevertheless, the estimates are bracketed by the in situ measurements of *Richter-Menge and Elder* [1998] and *Richter-Menge et al.* [2002], who reported ice sheet failure stresses during winter 1993–1994 of 100 to 300 kPa and during winter 1997–1998 of 10 to 60 kPa.

[31] The skeptic might argue that although order-of-magnitude agreement is evident, the agreement offers little support for the hypothesis of scale independence because the field features and the stress measurements were made at different times and in different sites. That concern may be lessened by the final example we cite at the end of the following section.

4. Formation Mechanism of Brittle Compressive Shear Faults

[32] We return now to the issue defined in section 1, namely, how do sliding lineaments/brittle compressive shear faults form within the sea ice cover? The Landsat-7 and Twin Otter features, although specific in terms of time and place, are examples, we believe, of the kind of fault that recurs throughout the Arctic Basin year after year at various periods throughout winter, judging from the literature mentioned in section 1. We take the view, therefore, that shear faults within the arctic sea ice cover share a common origin. More specifically, and as sketched in Figures 8a and 8b, we suggest that the field faults, like their laboratory counterparts [*Schulson et al.*, 1999], form through the initiation, growth, and interaction of secondary cracks that stem from thermal cracks and other primary stress concentrators. Upon forming en echelon arrays and lowering the shear resistance along certain macroscopic planes, the secondaries eventually link up, thereby forming the fault that destabilizes the cover.

[33] Direct evidence of this mechanism and of the role of secondary cracks may be seen in another time series of RADARSAT images, Figure 9, again provided by R. Kwok (Jet Propulsion Laboratory, personal communication, 2003) and reproduced with his permission. For an animation, see http://www-radar.jpl.nasa.gov/rgps/image_files/combine_small.gif, where clock-wise rotation is evident. The images were obtained during the 1997–1998 SHEBA experiment [*Perovich et al.*, 1999] and are centered on the SHEBA ice camp, whose coordinates in the Beaufort Sea on day 318 of 1997 were 76.1°N/145.8°W. Figure 9a shows the location of the SHEBA camp. Figure 9b was obtained on day 302 of 1997, Figure 9c on day 314, and Figure 9d on day 317. Figure 9e shows ice motion vectors that R. Kwok (Jet Propulsion Laboratory, personal communication, 2003) determined from displacement that occurred between days 314 and 317. Inhomogeneous deformation is evident from the distortion in the superimposed 50 km ×

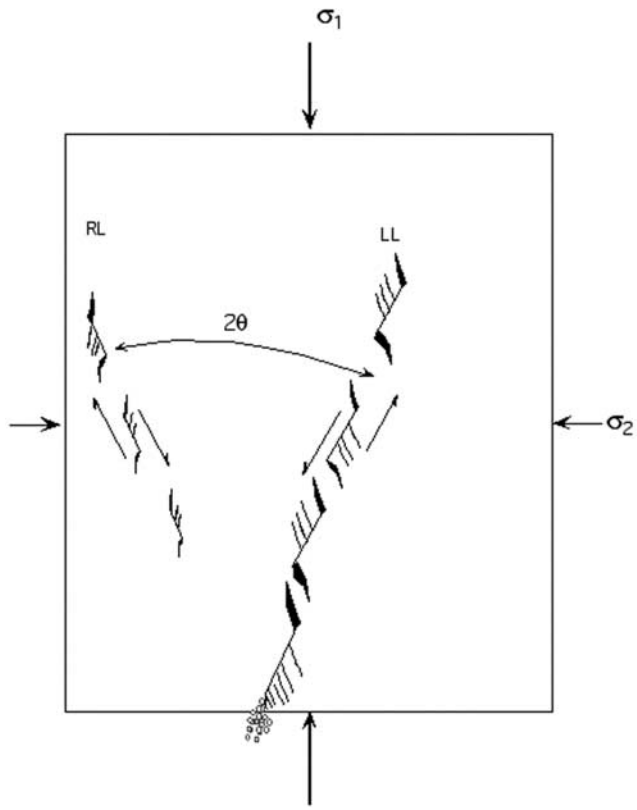

Figure 8b. Schematic sketch of proposed mechanism that triggers brittle compressive shear faulting via the linking of en echelon arrays of comb cracks.

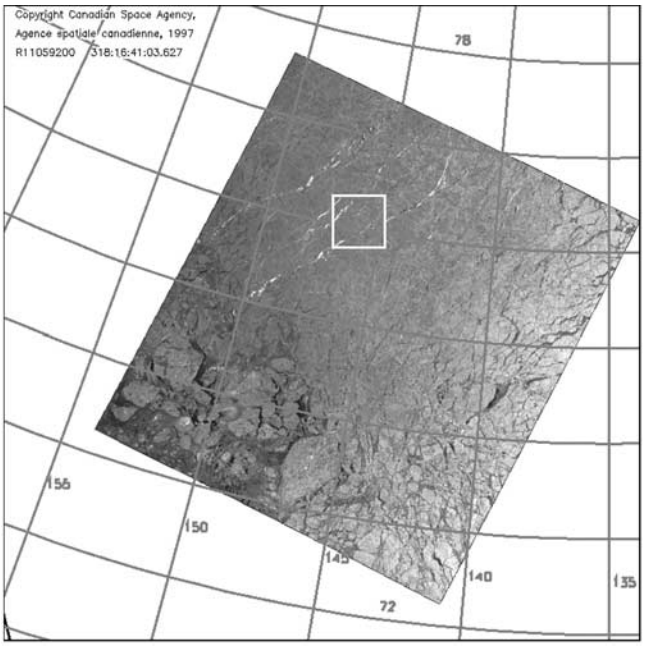

Figure 9a. RADARSAT image of sea ice taken during the SHEBA field experiment, courtesy of R. Kwok of Jet Propulsion Laboratory and Harry Stern, Applied Physics Laboratory, University of Washington. RADARSAT imagery (©CSA 2002). The SHEBA camp is centered (box in the image) showing the location of the scene in Figures 9b–9e. The image was taken on day 318 of 1997.

50 km boundary that surrounds the camp. Of interest to the present discussion are the two subparallel faults that formed between days 314 and 317, denoted A-A′ and B-B′ in Figure 9d. Both faults reflect discontinuities in the velocity gradients of Figure 9e, implying that the deformation was highly localized. The faults are characterized by left-lateral sliding and by moderate opening of the ice cover.

[34] Of particular interest is the en echelon pair of wing cracks that appear along fault B-B′ on either side of its intersection with the northern segment of the boundary. Wing-like cracks also define fault A-A′, although in this case they are distorted by the greater opening. Rhomboidal openings stemming from the wing cracks punctuate fault A-A′ as a result of the greater amount of relative sliding

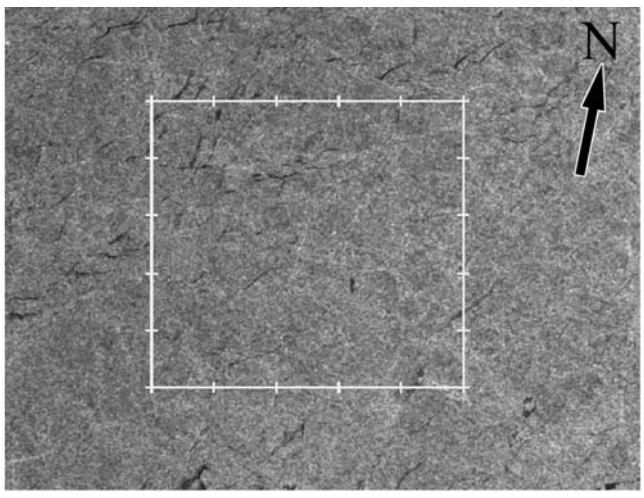

Figure 9b. RADARSAT image of sea ice taken during the SHEBA field experiment, courtesy of R. Kwok of Jet Propulsion Laboratory and Harry Stern, Applied Physics Laboratory, University of Washington. RADARSAT imagery (©CSA 2002). The image was taken on day 302 of 1997.

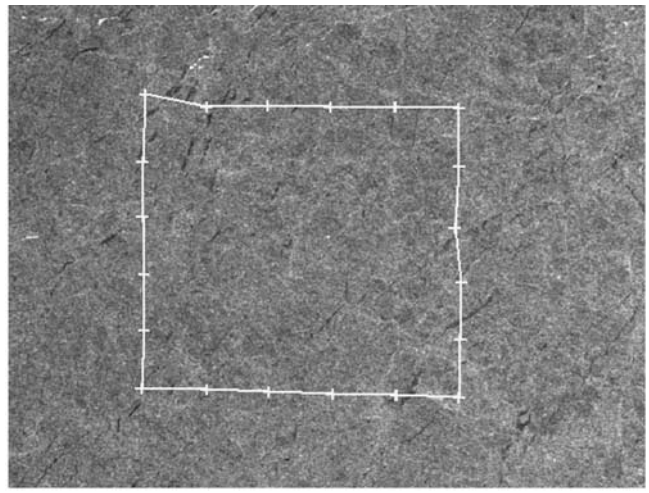

Figure 9c. RADARSAT image of sea ice taken during the SHEBA field experiment, courtesy of R. Kwok of Jet Propulsion Laboratory and Harry Stern, Applied Physics Laboratory, University of Washington. RADARSAT imagery (©CSA 2002). The image was taken on day 314 of 1997.

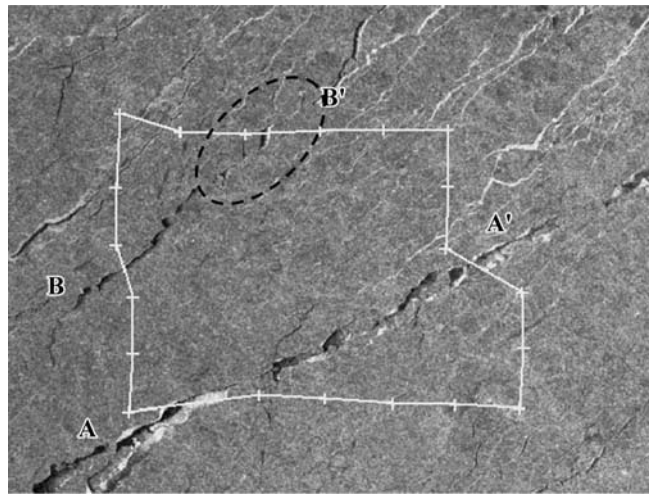

Figure 9d. RADARSAT image of sea ice taken during the SHEBA field experiment, courtesy of R. Kwok of Jet Propulsion Laboratory and Harry Stern, Applied Physics Laboratory, University of Washington. RADARSAT imagery (©CSA 2002). The image was taken on day 317 of 1997. Note the two left-lateral shear faults A-A′ and B-B′, the ''closed'' wing cracks on fault-B-B′ near to its intersection with the northern border (circled), and the rhomboidal openings along the more open fault A-A′.

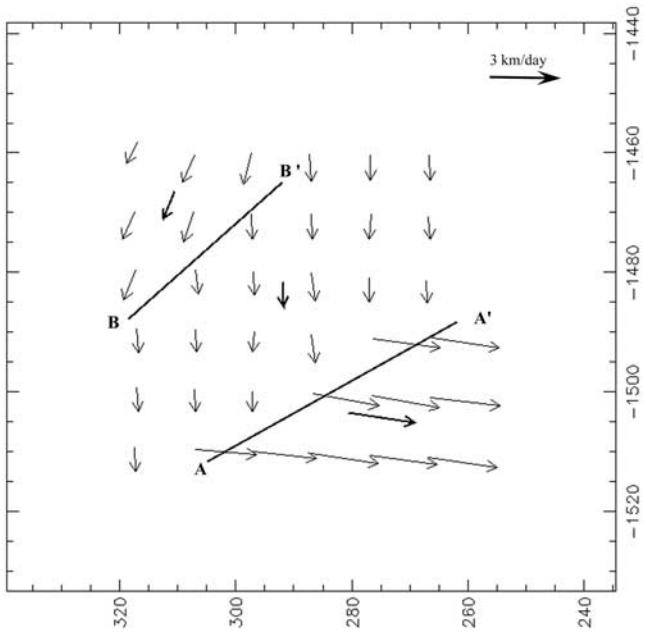

Figure 9e. RGPS (RADARSAT Geophysical Processor System) image of sea ice taken during the SHEBA field experiment, courtesy of R. Kwok of Jet Propulsion Laboratory and Harry Stern, Applied Physics Laboratory, University of Washington. RADARSAT imagery (©CSA 2002). Ice motion vectors from RGPS data of the deformation are localized around faults A-A′ and B-B′ for a time step of 3.0087 days between day 314 and 317 of 1997. The vectors are drawn on a Cartesian coordinate system with the origin at the North Pole; the x axis is parallel to the 45 east meridian and the y axis is parallel to the 145 east meridian. The numbers are in units of kilometers. The center of the plot is at approximately (−1480, 290) kilometers.

along it. Note also that the parent segments of the wing cracks that define fault A-A′ (Figure 9d) are visible in the image obtained 3 days earlier (Figure 9c), in keeping with the view that shear faults are the culmination of a multistage process that involves the linkage of cracks.

[35] An analysis of the deformation field around faults A-A′ and B-B′ is given in Appendix B and summarized in Tables 2 and 3. The analysis shows that the relative velocities and deformation rate are of similar magnitude as those reported in the literature for other arctic lineaments [e.g., see *Stern and Moritz*, 2002], implying that faults A-A′ and B-B′ are not atypical. The direction of maximum principal stress (again, the most compressive stress within the horizontal plane of the cover) was rotated counterclockwise about the average strike of the faults, by $\theta = 34.8° \pm 2.0°$ (Table 3). The rotation is consistent with the requirement of brittle compressive failure theory [*Jaeger and Cook*, 1979], and its c-c sense is consistent with the L-L character of the faults. Also, the more clearly defined wing cracks along fault B-B′ tend toward the principal direction, again as theory dictates [*Nemat-Nasser and Horii*, 1982; *Ashby and Hallam*, 1986].

Table 3. Calculation of the Direction of Maximum Principal Stress for the Two Faults Shown in Figure 9d From the Data in Table 2[a]

Fault	Strain Rate, day^{-1}			$\tan 2\alpha = \frac{2\dot{\varepsilon}_{xy}}{(\dot{\varepsilon}_{yy} - \dot{\varepsilon}_{xx})}$	α, deg
	$\dot{\varepsilon}_{xx}$	$\dot{\varepsilon}_{yy}$	$\dot{\varepsilon}_{xy}$		
A-A′	0	0.11	0.18	3.39	36.8
B-B′	0	0.029	0.032	2.17	32.7

[a]Relative to the strike of the fault the principal direction is rotated counterclockwise by $\alpha°$.

[36] We do not know why the angle between the faults and the direction of maximum principal stress is larger in this case than in the Landsat-7 scene nor, by implication from equation (1), why μ is lower. Guided again by the laboratory results, we think that the difference is not related to faulting along a single set vs. a conjugate set of planes. Could the ice have been warmer? Could the fault have been smoother.

[37] Finally, on the magnitude of the principal stress that led to the SHEBA faults, the geometry of the pair of wing cracks noted along fault B-B′ (i.e., $L \sim 0.8$ and $a \sim 3.5$ km) and equation (2) (again taking $K_c \sim 250$ kPa m$^{0.5}$ and $\mu_\kappa \sim 0.5$) lead to the estimate $\sigma_{1f} \sim 19$ kPa. This is similar to the stresses deduced above from wing cracks that formed within the ice cover at different times and places. More importantly, the estimate is also similar in magnitude to in situ measurements by *Richter-Menge et al.* [2002, Figure 1a] of compressive stress spikes of about 30 kPa around mid-November 1997 within the SHEBA vicinity, i.e., around the day that faults A-A′ and B-B′ were first observed.

[38] We recognize that this analysis is based upon few observations. Nevertheless, it offers additional support for our hypothesis that the physics of fracture of sea ice is independent of spatial scale. Hopefully, the work will stimulate further studies, at higher spatial and temporal resolution.

5. Questions Arising

[39] In interpreting long, sliding lineaments within the artic sea ice cover as brittle compressive shear faults and in

Table 2. Calculation of the Deformation Rate Localized Within the Vicinity of Faults A-A′ and B-B′ of Figure 9d, From RGPS Data Provided by R. Kwok

Fault	Relative Motion, km		Relative Velocity, km/d^{-1}		Partial Derivatives, day^{-1}				Deformation Rate, day^{-1}		
	Sliding Along Fault, u	Opening Normal to Fault, v	Sliding $\dot{u}$	Opening $\dot{v}$	$\frac{\partial u}{\partial x}$	$\frac{\partial v}{\partial y}$	$\frac{\partial u}{\partial y}$	$\frac{\partial v}{\partial x}$	Divergence	Shear	Vorticity
A-A′	11.02	3.25	3.66	1.08	0	0.11	0.36	0	0.11	0.38	0.36
B-B′	1.93	0.88	0.64	0.29	0	0.029	0.064	0	0.029	0.069	0.064

arguing that the failure of sea ice appears to obey scale-independent physics, several questions arise:

[40] 1. Why does the ice cover exhibit brittle behavior? One might have thought that a floating plate whose average temperature is >90% of its melting point and which on average deforms rather slowly would creep in the way that glaciers do, instead of breaking up. The answer, we think, can be found in a simple model of the ductile-to-brittle transition, as discussed below.

[41] 2. Why did conjugate faults form in the Landsat-7 scene (Figure 1) and not in the SHEBA scene (Figure 9)?

[42] 3. Do faults form sequentially during a given stress event, and what factors determine the spacing between them?

[43] 4. How much deformation damage is needed to trigger a new shear fault?

[44] 5. What are the limitations of the present interpretation and analysis?

[45] 6. What experiments are needed to further examine the hypotheses presented here?

[46] 7. What are the broader implications of the present results?

5.1. Ductile-Brittle(D/B) Transition

[47] In earlier discussions [*Schulson*, 1990; *Schulson and Nickolayev*, 1995] we examined the D/B transition under compression and proposed that it occurs when the rate of stress buildup at concentrators exceeds the rate of stress relaxation through creep. This led to the concept of a transition strain rate, $\dot{\varepsilon}_t$, above which inelastic behavior exhibits the characteristics of brittle deformation, namely, pressure-sensitive failure, the absence of strain rate hardening, dilatancy, and, of course, shear faulting. At lower rates, creep dominates the macroscopic deformation, characterized by pressure-insensitive failure, strain rate hardening, and more homogeneously distributed flow. Although inelastic deformation varies in both space and time within both regimes of behavior on both the large and small scales, the concept of critical strain rate is based upon an average rate, in the same way it is when describing constitutive relationships. Quantitatively, the transition strain rate can be described by the simple model [*Schulson*, 1990, 2001]

$$\dot{\varepsilon}_t = \frac{BK_c^3}{f\, d^{1.5}\left\{\left(1+\mu_k^2\right)^{0.5} - \mu_k - R\left(\mu_k + \left(1+\mu_k^2\right)^{0.5}\right)\right\}}, \qquad (4)$$

where B is the constant in the power law or dislocation creep equation ($\dot{\varepsilon} = B\sigma^n$ and $n = 3$), d is the size of the pre-existing stress concentrator, f is a geometrical factor of order 0.01, and K_c, μ_k, and R have the same meaning as above. For instance, at -10°C where $B = 5.1 \times 10^{-6}$ MPa^{-3} s^{-1} [*Sanderson*, 1988] and assuming $R = 0.05$, again taking $K_c = 250$ kPa m$^{0.5}$ and $\mu_k = 0.5$, a set of stress concentrators in the form, say, of randomly oriented thermal cracks of $d = 100$ m in length leads to a transition strain rate of $\dot{\varepsilon}_t = 1.6 \times 10^{-8}$ s^{-1}. Larger cracks of the kind commonly seen in the field [*Evans and Untersteiner*, 1971; M. D. Coon, personal communication, 2003] reduce this value. The point here is that the natural ice covers contain such large stress concentrators that at the average rate at which the covers deform, which depends somewhat upon scale (Marsan et al., submitted manuscript, 2004) but which for the present argument may be taken to be about 1%/day or 10^{-7} s^{-1} [*Kwok*, 2001], stress buildup at crack tips exceeds stress relaxation there, hence the brittle behavior.

[48] Incidentally, the above model is based upon scale-independent mechanisms. It contains only physical parameters that can be measured independently, i.e., no adjustable ones, and it has been shown through systematic experiment to work well on the laboratory scale (for a review, see *Schulson* [2001]). While simplistic in that it ignores primary and tertiary creep, crack interactions, heterogeneities, and possible differences in materials properties between the field and the laboratory, that it seems to work on the geophysical scale offers further support for the concept of scale-independent deformation physics.

[49] The transition strain rate, we note, is relatively low. One of the reasons is that as a material, ice exhibits relatively high creep resistance. This is evident from the fact that when at a temperature of 90% of its melting temperature and under a shear stress of $10^{-4}G$, where G is the shear modulus, ice creeps at $\sim 10^{-8}$ s^{-1}. This is to be compared, for instance, with a creep rate of $\sim 10^{-3}$ s^{-1} for elemental nickel and for the mineral wustite (FeO) at the same normalized temperature and stress [*Frost and Ashby*, 1982]. The low rate results from the fact that dislocations within the ice *Ih* crystal structure glide rather sluggishly through the lattice [*Shearwood and Whitworth*, 1991] owing, it has been suggested [*Glen*, 1968], to the unique requirement of protonic rearrangement. Another reason for the low transition strain rate is that the fracture toughness of ice is amongst the lowest of all materials.

5.2. Conjugate Faulting

[50] We do not know why conjugate faulting occurs in some situations and not in others. This also happens in the laboratory, as already noted. There we find that under ostensibly identical loading conditions, one set of specimens brought to terminal failure under biaxial compression fails by conjugate faulting, while another set fails along a single set of planes. Otherwise, the mechanical behavior and deformation damage are indistinguishable. As S. L. McNutt (University of Alaska-Fairbanks, personal communication, 2003) and one of the reviewers of the manuscript have pointed out, perhaps the proximity to boundaries such as coastlines and the one between the seasonal ice zone and the perennial ice zone is a key factor, in keeping with the fact from the present study that the Landsat-7 scene was nearer land than was the SHEBA scene. More fundamentally, and drawing upon the mechanics of strike-slip faulting within Earth's crust [*Sylvester*, 1988], conjugate faulting may signify pure shear (irrotational) deformation, while the lack of a conjugate set may signify simple shear (rotational) deformation, in keeping with the rotation within the SHEBA scene. More work is needed to elucidate this issue.

5.3. Sequence of Formation and Fault Spacing

[51] It is not possible from any of our observations to determine the order of fault formation during a given stress event, or even if there is one. About all that can be said, judging from the SHEBA scene (Figure 9) and from high-speed photographs taken in the laboratory [*Smith and Schulson*, 1993] is that subparallel faults seem to become

recognizable in a relatively short period of time; i.e., that following the buildup of internal stress and the attendant development of secondary cracks, mechanical instability sets in rather suddenly and generally along more than a single zone. What determines the spacing of the zones, or even if this is a fundamental characteristic given that higher-resolution data may reveal more closely spaced members, as in the Twin Otter scene, is not known.

5.4. A Critical Amount of Deformation Damage?

[52] In considering the onset of compressive shear faulting in rock, *Costin* [1983] proposed the concept of a critical density of deformation damage uniformly distributed. We argue against this idea, because studies in the laboratory have shown that when ice is slowly deformed (i.e., within the ductile regime) the deformation damage far exceeds that within the brittle regime [*Schulson*, 1990]. However, this does not rule out the possibility of a critical density of damage within a localized zone. Indeed, our suggestion that shear faults initiate when wing cracks link up or possibly when comb cracks become unstable is tantamount to suggesting a critical density within a narrow zone. We do not know, however, what that local density is. Again, more work is needed.

5.5. Limitations

[53] Up to this point in the paper, we have focused on relative sliding in a direction that is contained within the plane of loading, whether in the field or in the laboratory. By implication, this limits the discussion to moderate biaxial confinement; i.e., to loading/deformation paths along which the minor compressive stress, σ_2, is a small fraction of the major compressive stress, σ_1. Under higher biaxial confinement, S2 ice (defined in section 2.4) no longer exhibits significant inelastic deformation in the loading plane, but deforms through its thickness in the out-of-plane direction. At least, that is what happens in the laboratory [*Schulson and Nickolayev*, 1995] when ice is deformed within the regime of brittle behavior. The reason for the transition in the mode of failure is that the confining stress eventually becomes large enough to suppress in-plane frictional sliding. The ice still exhibits brittle behavior, but fails via out-of-loading-plane spalling [*Iliescu and Schulson*, 2004]. The criterion for the failure-mode transition is given by the relationship [*Schulson*, 2001]

$$R_c = \frac{(1+\mu^2)^{0.5} - \mu}{(1+\mu^2)^{0.5} + \mu}, \tag{5}$$

where R_c denotes a critical value of the stress ratio $R = \sigma_2/\sigma_1$. If the same thing happens in the field, then one would expect to find certain lineaments that do not exhibit relative shear movement in the plane of the cover, but only divergence once the loading event ends and the cover opens up. For instance, in situations where the friction coefficient is as high as $\mu = 1.7$, the largest value deduced from the Landsat-7 scene (section 3.2), the confinement need only be as high as R = 0.07 to effect this failure-mode transition. Perhaps the nonshearing linear kinematic features that *Kwok* [2001] observed and the nonsheared lineaments L2 and L10 that we observed in the Landsat-7 scene (section 2.1) originated through out-of-plane faulting, in the manner of a thrust fault within Earth's crust.

[54] The discussion is also limited to a pattern of deformation that develops within a damaged continuum, and thus to events during winter at higher latitudes within the Arctic Basin where the ice is more compact and more often under compression. During summer at lower latitudes, melting of thinner ice creates individual floes whose collective behavior is probably better considered within the context of granular media.

5.6. Next Tests

[55] To further examine the hypotheses presented here, we suggest the following experiments:

[56] 1. In the laboratory, determine whether a reduction in temperature reduces the intersection angle of conjugate faults, and determine whether a new set of in-loading-plane faults develops upon either rotating a faulted specimen by about 90° with respect to the direction of maximum principal stress or rotating the principal stress direction, care being taken to quantify the effects of fault healing. Also, determine whether boundary conditions and whether loading along paths of constant principal strain ratio versus paths of constant principal stress ratio (as done to date) affect the incidence of conjugate faulting. In addition, determine the coefficient of internal friction for damaged ice by performing sliding experiments along naturally formed faults.

[57] 2. In the field, make satellite observations at higher spatial and temporal resolution. Also, determine whether the maximum principal stress and strain directions, measured on the spatial scale of the fracture features, correlate with the orientation of secondary cracks and sliding lineaments. Also, measure in situ stresses at higher temporal resolution to see whether short-term stress events occur of MPa magnitude, and, if possible, determine whether nonsliding lineaments during their formation exhibit greater relative movement in the direction normal to the plane of the cover than do sliding lineaments.

5.7. Broader Implications

[58] In identifying sea ice sliding lineaments as brittle compressive fracture features, we reiterate the fact, discussed by *Stern and Rothrock* [1995] from an analysis of SAR data, that failure occurs through highly localized as opposed to uniformly distributed deformation. The localization is important to an understanding of the ice thickness distribution and, ultimately, to better modeling of the role of ice mechanics on the arctic climate system. Scale invariance, we believe, may be key to a better understanding of sea ice deformation on all scales, an understanding that is becoming increasingly important as the spatiotemporal resolution of numerical models approaches the kilometer/subkilometer and daily/subdaily scales. In a broader sense, and in keeping with recent developments [*Renshaw and Schulson*, 2001], a better understanding of mechanisms underlying sea ice fracture may help to elucidate the failure of Earth's crust, for faulting of the lithosphere is also characterized by deformation features that look alike on different scales [*Allègre et al.*, 1982]. Sea ice may also help to understand the icy crust of Europa [*Greeley et al.*, 1998] which, while floating on a putative ocean [*Carr et al.*, 1998], fractures

under loads induced through diurnal tides and nonsynchronous rotation [*Greenberg and Weidenschilling*, 1984] via, amongst other modes, wing-like cracking [*Schulson*, 2002b] and possibly brittle compressive shear faulting [*Schenk and Mckinnon*, 1989; *Spaun et al.*, 2001].

6. Conclusions

[59] From an examination of fracture features within the winter sea ice cover on the Arctic Ocean, as seen via satellite imagery, an aerial survey, and laboratory experiments, we conclude the following:

[60] 1. Deformation features are remarkably similar in appearance over the range of spatial scale from kilometers to millimeters. This look alikeness and the order-of-magnitude agreement between the stress calculated to create secondary cracks and the stresses measured within the winter ice cover by *Richter-Menge and Elder* [1998] and *Richter-Menge et al.* [2002] support the hypothesis that contrary to hierarchy theory, the basic failure mechanisms are scale invariant and operate on many scales.

[61] 2. Sliding lineaments within the sea ice cover form under a far-field compressive stress state, sometimes as conjugate sets, where the failure planes are inclined at an angle of less than 45° to the direction of maximum (most compressive) principal stress and on either side of it, analogous to strike-slip faults within the Earth's crust. We identify the lineaments as brittle compressive shear faults.

[62] 3. Brittle compressive shear faults are created through the linking up of deformation-induced secondary cracks, under a level of stress that increases as the size of the stress concentrator decreases.

Appendix A: Elastic Buckling of an Ice Sheet

[63] To evaluate elastic buckling, we assumed that a floating ice sheet can be modeled as a plate on an elastic foundation, and then applied *Kerr*'s [1978] analysis of the problem, which is summarized by *Sanderson* [1988]. Accordingly, the stress to cause buckling of a sheet of thickness, t, of Young's modulus, E, and Poisson's ratio, υ, loaded essentially uniaxially and under the restorative force arising from the potential energy gradient is given by the relationship

$$\sigma_b = 2.6\left[Et\rho_w g/12\left(1-\upsilon^2\right)\right]^{0.5},$$

where ρ_w is the density of seawater and g is the acceleration of gravity. Upon inserting appropriate values of the parameters (ρ_w = 1028 kg/m^3, g = 9.8 m/s^2, υ = 0.3, and $E \sim 8$ GPa [*Langleben and Pounder*, 1963] for "cold" sea ice), we find that for a sheet of thickness 1.8 m to 2.8 m the elastic buckling stress is expected to be $\sigma_b \sim 0.3$, $b \sim 10-12$ MPa.

Appendix B: Deformation and Principal Axes Determined From Ice Motion Vectors

[64] To quantify the deformation manifested by the faults in Figures 9d and 9e, we made calculations of divergence and shear as well as vorticity, using displacement data provided by R. Kwok (personal communication, 2003) of JPL. We assumed that the ice sheet is a 2-D body and then determined the direction of principal stress, first by computing the direction of principal strain and then by assuming that the ice cover was mechanically isotropic so that the two directions were parallel to each other. We made the calculations as follows:

[65] We defined a Cartesian coordinate system, x-y, centered on a fault (e.g., on fault A-A′, Figure 9d), and denoted the relative displacements along and perpendicular to the fault, respectively, by u and v. We let the velocity of the floe below each fault be zero; i.e., $u = v = 0$ for $y < 0$. Table 2 lists the deformation rate for faults A-A′ and B-B′ of Figure 9d as well the velocities u and v, which were computed by assuming that the displacement occurred over a period of 3.0087 days. To obtain the partial derivatives $\partial u/\partial x$, $\partial v/\partial y$, $\partial u/\partial y$, and $\partial v/\partial x$ from which the deformation (divergence and shear) and the vorticity were calculated, we assumed a "sample size" of 10 km, which is the size of the grid in Figure 9. The partials in x parallel to the faults are zero by definition. Table 2 lists these derivatives. From the definitions

$$D = (\partial u/\partial x + \partial v/\partial y), \tag{B1}$$

$$S = \left([\partial u/\partial x - \partial v/\partial y]^2 + [\partial u/\partial y + \partial v/\partial x]^2\right)^{0.5}, \tag{B2}$$

$$V = (\partial v/\partial x - \partial u/\partial y), \tag{B3}$$

where D is divergence, S is shear, and V is vorticity, we obtained the values listed in the last three columns of Table 2.

[66] The analysis shows that there are significant differences across the scene. Clearly the deformation is not uniform, but highly localized. Nevertheless, we retain the concept of strain to allow the principal direction of strain to be determined, although the principal direction does not depend upon the sample size. From the components of the strain rate tensor defined as

$$\dot{\varepsilon}_{xx} = \partial u/\partial x = 0, \tag{B4}$$

$$\dot{\varepsilon}_{yy} = \partial v/\partial y, \tag{B5}$$

$$\dot{\varepsilon}_{xy} = (\partial u/\partial y + \partial v/\partial x)/2 = (\partial u/\partial y)/2, \tag{B6}$$

and listed in Table 3, we obtained the angle, α, between the strike of the fault and the direction of the maximum principal strain (taken as the most compressive strain) from the relationship

$$\tan 2\alpha = 2\dot{\varepsilon}_{xy}/\left(\dot{\varepsilon}_{xx} - \dot{\varepsilon}_{yy}\right) = -u/v. \tag{B7}$$

For both faults shown in Figure 9d, the principal strain direction is counterclockwise from the strike of the fault, by 36.8° for fault-A and by 32.7° for fault-B.

[67] **Acknowledgments.** We acknowledge Jackie Richter-Menge, Harold Frost, Ronald Kwok, Lyn McNutt, James Overland, and Jerome Weiss for helpful discussions. As noted in the text, Ronald Kwok provided Figures 5a, 9b, 9c, 9d, and 9e as well as the RGPS data listed in Table 2, and Harry Stern of University of Washington provided Figure 9a. We also acknowledge the helpful comments by the reviewers of this manuscript.

Fred Karig and his colleagues of the University of Washington harvested the ice from the ICEX03 camp, and Andrew Fortt of Dartmouth assisted with the aerial study and with the laboratory measurements. The work was supported by National Oceanographic and Atmospheric Administration (grant NA17RP1400), the National Science Foundation (grant OPP-0328605), and Office of Naval Research through ICEX03.

References

Allègre, C. J., J. L. Le Mouel, and A. Provost (1982), Scaling rules in rock fracture and possible implications for earthquake prediction, *Nature*, *297*, 47–49.

Ashby, M. F., and S. D. Hallam (1986), The failure of brittle solids containing small cracks under compressive stress states, *Acta Metall.*, *34*, 497–510.

Brace, W. F., and E. G. Bombolakis (1963), A note of brittle crack growth in compression, *J. Geophys. Res.*, *68*(12), 3709–3713.

Carr, M. H., et al. (1998), Evidence for a subsurface ocean on Europa, *Nature*, *391*, 363–365.

Cooke, M. L. (1997), Fracture localization along faults with spatially varying friction, *J. Geophys. Res.*, *102*(B10), 22,425–22,434.

Coon, M. D., G. S. Knoke, and D. C. Echert (1998), The architecture of an anisotropic elastic-plastic sea ice mechanics constitutive law, *J. Geophys. Res.*, *103*(C10), 21,915–21,925.

Costin, L. S. (1983), A microcrack model for the deformation and failure of brittle rock, *J. Geophys. Res.*, *88*(B11), 9485–9492.

Dempsey, J. P. (1996), Scale effects on the fracture of ice, in *The Johannes Weertman Symposium*, edited by R. J. Arsenault et al., pp. 351–361, Min., Metals and Mat. Soc., Anaheim, Calif.

Dykins, J. E. (1970), Ice engineering: Tensile properties of sea ice grown in a confined system, *Tech. Rep. R689*, Nav. Civ. Eng. Lab., Port Hueneme, Calif.

Erlingsson, B. (1988), Two-dimensional deformation patterns in sea ice, *J. Glaciol.*, *34*, 301–308.

Erlingsson, B. (1991), The propagation of characteristics in sea-ice deformation fields, *Ann. Glaciol.*, *15*, 73–80.

Evans, R. J., and N. Untersteiner (1971), Thermal cracks in floating ice sheets, *J. Geophys. Res.*, *76*(3), 694–703.

Fortt, A., and E. M. Schulson (2004), Post-terminal compressive deformation of ice: Friction along coulombic shear faults, *Eos. Trans. AGU*, *85*(17), Joint Assembly Suppl., Abstract T13A-05.

Fortt, A., E. M. Schulson, and E. Russell (2003), Sliding along Coulombic shear faults in ice, *Can. J. Phys.*, *81*, 519–527.

Frost, H. J., and M. F. Ashby (1982), *Deformation Mechanisms Maps*, Pergamon, New York.

Glen, J. W. (1968), The effect of hydrogen disorder on dislocation movement and plastic deformation in ice, *Phys. Kondens. Mater.*, *7*, 43–51.

Greeley, R., et al. (1998), Terrestrial sea ice morphology: Considerations for Europa, *Icarus*, *135*, 25–40.

Greenberg, R. P., and S. J. Weidenschilling (1984), How fast do Galilean satellites spin?, *Icarus*, *58*, 186–196.

Hibler, W. D., and E. M. Schulson (2000), On modeling the anisotropic failure and flow of flawed sea ice, *J. Geophys. Res.*, *105*(C7), 17,105–17,120.

Hutchings, J. K., and W. D. Hibler (2002), Modelling sea ice deformation with a viscous-plastic isotropic rheology, in *Ice in the Environment: Proceedings of the 16th Ice Symposium*, pp. 358–366, Int. Assoc. of Hydraul. Res., Dunedin, New Zealand.

Iliescu, D., and E. M. Schulson (2004), The brittle compressive failure of fresh-water columnar ice loaded biaxially, *Acta Mater.*, in press.

Jaeger, J. C., and N. G. W. Cook (1979), *Fundamentals of Rock Mechanics*, pp. 95–100, Chapman and Hall, New York.

Kennedy, F. E., E. M. Schulson, and D. Jones (2000), Friction of ice on ice at low sliding velocities, *Philos. Mag. A*, *80*(5), 1093–1110.

Kerr, A. D. (1978), On the determination of horizontal forces a floating ice sheet exerts on a structure, *Rep. 78-15*, Cold Reg. Res. and Eng. Lab., Hanover, N. H.

Kuehn, G. A., R. W. Lee, W. A. Nixon, and E. M. Schulson (1990), The structure and tensile behavior of first-year sea ice and laboratory-grown saline ice, *J. Offshore Mech. Arct. Eng.*, *112*, 357–363.

Kwok, R. (1998), The RADARSAT Geophysical Processor System, in *Analysis of SAR Data of the Polar Oceans*, edited by C. Tsatsoulis and R. Kwok, pp. 235–257, Springer-Verlag, New York.

Kwok, R. (2001), Deformation of the Arctic Ocean sea ice cover between November 1996 and April 1997: A qualitative study, in *Scaling Laws in Ice Mechanics*, edited by J. P. Dempsey and H. H. Shen, pp. 315–322, Kluwer Acad., Norwell, Mass.

Kwok, R., D. A. Rothrock, H. L. Stern, and G. F. Cunningham (1995), Determination of ice age using Lagrangian observations of ice motion, *IEEE Trans. Geosci. Remote Sens.*, *33*(2), 392–400.

Langleben, M. P., and E. R. Pounder (1963), Elastic parameters of sea ice, in *Ice and Snow-Processes, Properties and Applications*, edited by W. E. Kingery, pp. 69–78, MIT Press, Cambridge, Mass.

Laxon, S., N. Peacock, and D. Smith (2003), High interannual variability of sea ice thickness in the Arctic region, *Nature*, *425*, 947–950.

Lindsay, R. W., and D. A. Rothrock (1995), Arctic sea-ice leads from advanced very high-resolution radiometer images, *J. Geophys. Res.*, *100*(C3), 4533–4544.

Marko, J. R., and R. E. Thomson (1977), Rectilinear leads and internal motions in the ice pack of the western Arctic ocean, *J. Geophys. Res.*, *82*, 979–987.

Maykut, G. A. (1982), Large-scale heat exchange and ice production in the central Arctic, *J. Geophys. Res.*, *87*(C9), 7971–7984.

McNutt, S. L., and J. E. Overland (2003), Spatial hierarchy in Arctic sea ice dynamics, *Tellus, Ser. A*, *55*(2), 181–191.

Michel, B., and R. O. Ramseier (1971), Classification of river and lake ice, *Can. Geotech. J.*, *8*(36), 36–45.

Moritz, R. E., and H. L. Stern (2001), Relationship between geostrophic winds, ice strasin rates and the piecewise rigid motions of pack ice, in *Scaling Laws in Ice Mechanics*, edited by J. P. Dempsey and H. H. Shen, pp. 335–348, Kluwer Acad., Norwell, Mass.

Muehlberger, W. R. (1961), Conjugate joint sets of small dihedral angle, *J. Geol.*, *69*(2), 211–219.

Nemat-Nasser, S., and H. Horii (1982), Compression-induced non-planar crack extension with application to splitting, exfoliation, and rockburst, *J. Geophys. Res.*, *87*(B8), 6805–6821.

O'Neill, R. V., D. L. DeAngelis, J. B. Waide, and T. F. H. Allen (1986), *A Hierarchical Concept of Ecosystems*, Princeton Univ. Press, Princeton, N. J.

Overland, J. E., B. A. Walter, T. B. Curtin, and P. Turet (1995), Hierachy and sea ice mechanics: A case study from the Beaufort Sea, *J. Geophys. Res.*, *100*(C3), 4559–4571.

Overland, J. E., S. L. McNutt, S. Salo, and S. S. Li (1998), Arctic sea ice as a granular plastic, *J. Geophys. Res.*, *103*(C10), 21,845–21,867.

Perovich, D. K., et al. (1999), Year on the ice gives climate insights, *Eos Trans. AGU*, *80*(481), 485–486.

Renshaw, C. E., and E. M. Schulson (2001), The universal behavior in compressive failure of brittle materials, *Nature*, *412*, 897–900.

Richter-Menge, J. A., and B. C. Elder (1998), Characteristics of pack ice stress in the Alaskan Beaufort Sea, *J. Geophys. Res.*, *103*(C10), 21,817–21,829.

Richter-Menge, J. A., S. L. McNutt, J. E. Overland, and R. Kwok (2002), Relating arctic pack ice stress and deformation under winter conditions, *J. Geophys. Res.*, *107*(C10), 8040, doi:10.1029/2000JC000477.

Rothrock, D. A., and A. S. Thorndike (1984), Measuring the sea ice-floe size distribution, *J. Geophys. Res.*, *89*(C4), 6477–6486.

Rudnicki, J. W., and J. R. Rice (1975), Conditions for the localization of deformation in pressure-sensitive dilatant materials, *J. Mech. Phys. Solids*, *23*, 371–394.

Sanderson, T. J. O. (1988), *Ice Mechanics: Risks to Offshore Structures*, 147 pp., Graham and Trotman, London.

Schenk, P. M., and W. B. McKinnon (1989), Fault offsets and lateral crustal movement on Europa—Evidence for a mobile ice shell, *Icarus*, *79*, 75–100.

Scholz, C. H. (1990), *The Mechanics of Earthquakes and Faulting*, Cambridge Univ. Press, New York.

Schulson, E. M. (1990), Brittle compressive fracture of ice, *Acta Metall. Mater.*, *38*, 1963–1976.

Schulson, E. M. (2001), Brittle failure of ice, *Eng. Fracture Mech.*, *68*, 1839–1887.

Schulson, E. M. (2002a), Compressive shear faulting in ice: Plastic vs. Coulombic faults, *Acta Mater.*, *50*, 3415–3424.

Schulson, E. M. (2002b), On the origin of a wedge crack within the icy crust of Europa, *J. Geophys. Res.*, *107*(E11), 5107, doi:10.1029/2001JE001586.

Schulson, E. M., and W. D. Hibler (1991), The fracture of ice on scales large and small: Arctic leads and wing cracks, *J. Glaciol.*, *37*, 319–323.

Schulson, E. M., and W. D. Hibler (2004), Fracture of the winter sea ice cover on the Arctic Ocean, *C. R. Phys.*, in press.

Schulson, E. M., and O. Y. Nickolayev (1995), Failure of columnar saline ice under biaxial compression: Failure envelopes and the brittle-to-ductile transition, *J. Geophys. Res.*, *100*(B11), 22,383–22,400.

Schulson, E. M., D. Iliescu, and C. E. Renshaw (1999), On the initiation of shear faults during brittle compressive failure: A new mechanism, *J. Geophys. Res.*, *104*(B1), 695–705.

Shearwood, C., and R. W. Whitworth (1991), The velocity of dislocations in ice, *Philos. Mag. A*, *64*(2), 289–302.

Smith, T. R., and E. M. Schulson (1993), The brittle compressive failure of fresh-water columnar ice under biaxial loading, *Acta Metall. Mater.*, *41*, 153–163.

Spaun, N. A., R. T. Pappalardo, J. W. Head, and N. D. Sherman (2001), Characteristics of the trailing equatorial quadrant of Europa from Galileo imaging data: Evidence for shear failure in forming lineae, paper presented at Lunar Planetary Science Conference XXXII, Lunar and Planet. Inst., Houston, Tex.

Stern, H. L., and R. E. Moritz (2002), Sea ice kinematics and surface properties from RADARSAT synthetic aperture radar during the SHEBA drift, *J. Geophys. Res.*, *107*(C10), 8028, doi:10.1029/2000JC000472.

Stern, H. L., and D. A. Rothrock (1995), Open water production in Arctic sea ice: Satellite measurements and model parameterizations, *J. Geophys. Res.*, *100*(C10), 20,601–20,612.

Sylvester, A. G. (1988), Strike-slip faults, *Geol. Soc. Am. Bull.*, *100*, 1666–1703.

Vavrus, S. J., and S. P. Harrison (2003), The impact of sea ice dynamics on the Arctic climate system, *Clim. Dyn.*, *20*(7–8), 741–757.

Walter, B. A., and J. E. Overland (1993), The response of lead patterns in the Beaufort Sea to storm-scale wind forcing, *Ann. Glaciol.*, *17*, 219–226.

Walter, B. A., J. E. Overland, and P. Turet (1995), A comparison of satellite-derived and aircraft-measured regional surface sensible heat fluxes over the Beaufort Sea, *J. Geophys. Res.*, *100*(C3), 4585–4591.

Weiss, J. (2001), Fracture and fragmentation of ice: A fractal analysis of scale invariance, *Eng. Fracture Mech.*, *68*, 1975–2012.

Weiss, J. (2003), Scaling of fracture and faulting of ice on Earth, *Surv. Geophys.*, *24*, 185–227.

Weiss, J., and M. Gay (1998), Fracturing of ice under compression creep as revealed by a multifractal analysis, *J. Geophys. Res.*, *103*(B10), 24,005–24,016.

Zhang, J., D. A. Rothrock, and M. Steele (2000), Recent changes in Arctic sea ice: The interplay between ice dynamics and thermodynamics, *J. Clim.*, *13*, 3099–3114.

E. M. Schulson, Ice Research Laboratory, Thayer School of Engineering, Dartmouth College, Hanover, NH 03755, USA. (erland.schulson@dartmouth.edu)